

Lattice dynamics of the $\text{Ta}_2\text{Ni}(\text{Se}_{1-x}\text{S}_x)_5$ excitonic insulator

Mai Ye,^{1,*} Pavel A. Volkov,^{1,†} Himanshu Lohani,² Irena Feldman,²
Minsung Kim,¹ Amit Kanigel,² and Girsh Blumberg^{1,3,‡}

¹*Department of Physics and Astronomy, Rutgers University, Piscataway, NJ 08854, USA*

²*Department of Physics, Technion - Israel Institute of Technology, Haifa 32000, Israel*

³*National Institute of Chemical Physics and Biophysics, 12618 Tallinn, Estonia*

(Dated: July 20, 2021)

Recently, we employed electronic polarization-resolved Raman spectroscopy to reveal the strongly correlated excitonic insulator (EI) nature of Ta_2NiSe_5 [Volkov *et al.*, [npj Quant. Mater.](#) **6**, 52 (2021)], and also showed that for $\text{Ta}_2\text{Ni}(\text{Se}_{1-x}\text{S}_x)_5$ alloys the critical excitonic fluctuations diminish with sulfur concentration x exposing a cooperating lattice instability that takes over for large x [Volkov *et al.*, [arXiv:2104.07032](#)]. Here we focus on the lattice dynamics of the EI family $\text{Ta}_2\text{Ni}(\text{Se}_{1-x}\text{S}_x)_5$ ($x = 0, \dots, 1$). We identify all Raman-active optical phonons of A_g (fully symmetric) and B_{2g} (*ac*-quadrupole-like) symmetries (D_{2h} point group) and study their evolution with temperature and sulfur concentration. We demonstrate the change of selection rules at temperatures below the orthorhombic-to-monoclinic transition at $T_c(x)$ that is related to the EI phase. We find that $T_c(x)$ decrease monotonically from 328 K for Ta_2NiSe_5 to 120 K for Ta_2NiS_5 and that the magnitude of lattice distortion also decreases with the sulfur concentration x . For $x < 0.7$, the two lowest-frequency B_{2g} phonon modes show strongly asymmetric lineshapes at high temperatures due to Fano interference with the broad excitonic continuum present in a semimetallic state. Within the framework of extended Fano model, we develop a quantitative description of the interacting exciton-phonon excitation lineshape, enabling us to derive the intrinsic phonon parameters and determine the exciton-phonon interaction strength, that affects the transition temperature $T_c(x)$. While at low temperatures the intrinsic phonon parameters are in good agreement with the *ab initio* calculations and the anharmonic decay model, their temperature dependencies show several anomalous behaviors: (i) Frequencies of B_{2g} phonons harden pronouncedly upon cooling in vicinity of $T_c(x)$ for $x < 0.7$ semimetals and, in contrast, soften monotonically for Ta_2NiS_5 semiconductor; (ii) The lifetime of certain phonons increases strongly below $T_c(x)$ for $x < 0.7$ revealing the gap opening in the broken symmetry phase; (iii) For most modes, the intensity shows rather strong temperature dependence that we relate to the interplay between electronic and phononic degrees of freedom. For Ta_2NiSe_5 we also observe signatures of the acoustic mode scattered assisted by the structural domain walls formed below T_c . Based on our results, we additionally present a consistent interpretation of the origin of oscillations observed in time-resolved pump-probe experiments.

I. INTRODUCTION

In a narrow-gap semiconductor or semimetal, if the exciton binding energy exceeds the band gap, the Coulomb attraction between electrons and holes favors spontaneous formation of a macroscopic number of excitons. These bosonic quasiparticles then form a coherent state, opening an interaction-induced gap and leading to an insulating phase, named excitonic insulator [1–3]. If the electron and hole states belong to bands of different symmetry, the resulting excitonic insulator state is expected to break the crystal lattice symmetry.

Consider the case of a semimetal. If the band gap is indirect, i.e. the valence band maximum and the conduction band minimum are located at different places in the k -space, condensation of excitons leads to a charge-density-wave (CDW) state and accompanying crystal distortion which breaks translational symmetry [3]. The CDW wavevector is then given by the spanning vector

that connects the valence band maximum to the conduction band minimum. One such example is semimetal 1T-TiSe₂, which has been proposed to hold an excitonic insulating state below 190 K [4–7]. In contrast, if the band gap is direct, excitonic condensation only results in lattice distortion which breaks point-group symmetry. In this situation, the size of the unit cell does not change but its shape changes. Ta_2NiSe_5 is a candidate for excitonic insulator of this kind.

Ta_2NiSe_5 shows a second-order structural phase transition at $T_c = 326$ K [8, 9]. In the high temperature phase, this material has a orthorhombic structure (point group D_{2h}); in the low-temperature phase, the structural is monoclinic (point group C_{2h}) with the angle β between a and c directions deviating from 90° , Fig. 1. Below T_c , the valence-band top flattens as discovered by angle-resolved photoemission spectroscopy (ARPES) studies [10–12]. Band flatness at low temperature is viewed as a characteristic feature of the excitonic insulator ground state. Moreover, studies of nonequilibrium dynamics have demonstrated photoinduced enhancement of excitonic order [13, 14], photoinduced multistage phase transitions [15], ultrafast reversal of excitonic order [16], and coherent order-parameter oscillations [17].

* mye@physics.rutgers.edu

† pv184@physics.rutgers.edu

‡ girsh@physics.rutgers.edu

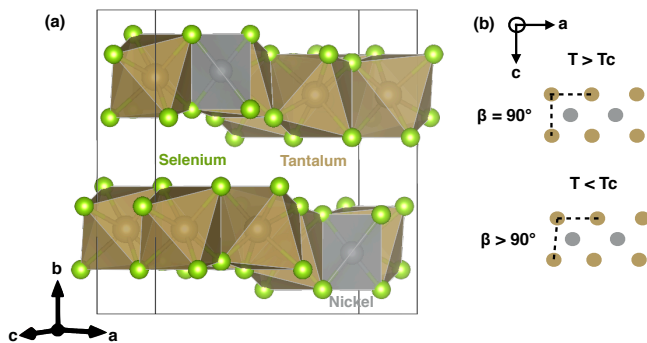


FIG. 1. Crystal structure of Ta_2NiSe_5 . The frame in (a) indicates the unit cell.

The lattice degrees of freedom play an important role in the physics of Ta_2NiSe_5 . In particular, the orthorhombic-to-monoclinic structural change can be induced via electron-phonon coupling [18] even if the origin of the transition is excitonic [19]. Moreover, a recent study combining ultrafast experiments with calculations proposes that the phase transition in Ta_2NiSe_5 is structural in its nature [20]. Thus, understanding the underlying physics of excitonic insulator candidates requires the lattice dynamics to be examined in a detailed way. Interestingly, substitution of Se with S results in a whole family of compounds $\text{Ta}_2\text{Ni}(\text{Se}_{1-x}\text{S}_x)_5$, where the orthorhombic-to-monoclinic transition has been suggested to be suppressed with x [8]. While it is known, that S substitution leads to an enhanced direct band gap [21], which is detrimental to the EI state, its effects on the lattice modes has not been systematically studied.

Because the inversion symmetry of $\text{Ta}_2\text{Ni}(\text{Se}_{1-x}\text{S}_x)_5$ is preserved across T_c , the soft mode of this zero-wavevector structural transition, if any, is Raman active. Polarization resolved low frequency Raman spectroscopy, therefore, is particularly suitable for studying the physics of the phase transition, and for evaluating the contribution of the lattice vibrations to the transition. This experimental method offers both the high energy resolution and the ability to selectively probe bosonic excitations in different symmetry channels [22].

In this work, we present a systematic study of the lattice dynamics for the family of $\text{Ta}_2\text{Ni}(\text{Se}_{1-x}\text{S}_x)_5$ ($x = 0, 0.25, 0.67, \text{ and } 1$) pristine crystals and alloys to quantitatively explore the spectral parameters of the phonons. We find the change of selection rules, indicating an orthorhombic-to-monoclinic structural transition at $T_c(x)$, which is finite for all x . The transition temperature $T_c(x)$ and the magnitude of lattice distortion both decrease with sulfur concentration x .

For $\text{Ta}_2\text{Ni}(\text{Se}_{1-x}\text{S}_x)_5$ with $x \leq 0.67$, the two lowest-energy symmetry-breaking B_{2g} phonon modes exhibit strong asymmetric lineshape above the transition temperature, resulting from the coupling between these modes and an excitonic continuum of the same symmetry. We develop an extended model to analyze the physics of

this Fano-type interference effect. Using this model, we disentangle the excitonic and phononic contributions to the Raman response, and illustrate the effect of the coupling between them: apart from renormalizing the bare phononic and excitonic responses, this effect also results in an additional interference term in the total Raman response. We find that the B_{2g} phonon modes exhibit no intrinsic softening on cooling towards the transition temperature. In contrast, the excitonic response shows clear soft-mode behavior [23, 24]. Additionally, many modes exhibit an anomalous increase in linewidth above T_c , suggesting the closing of the EI gap. For Ta_2NiSe_5 below T_c , we also observe signatures of the acoustic excitations with finite momenta, enabled by the formation of a quasi-periodic structure of domain walls.

For Ta_2NiS_5 , on the contrary, the phonon modes in the symmetry-breaking channel maintain symmetric lineshape, but their frequency anomalously decreases upon cooling. Because the structural change for Ta_2NiS_5 is very weak, no anomaly of phonon frequency or width is detected around its structural transition temperature.

For all compositions, we find that most phonons exhibit strong dependence of their intensity on temperature, and present arguments in favor of this being a result of a coupling to electronic excitations.

Additionally, we perform density functional theory (DFT) calculations of the lattice dynamics for Ta_2NiSe_5 and Ta_2NiS_5 . The phonon frequencies agree well with the experiment, and the obtained displacement patterns of the optical modes allow to explain the differences of the couplings of the three non-symmetric phonons to the excitonic continuum.

Finally, we demonstrate that our results are consistent with the modes observed in time-resolved experiments. We show however, that the signatures of the Fano-shaped phonons and the excitonic continuum above T_c may be hard to observe in that type of experiments.

The rest of this paper is organized as follows. In Sec. II we describe the sample preparation and experimental setup. In Sec. III we show an overview of the phonon spectra of $\text{Ta}_2\text{Ni}(\text{Se}_{1-x}\text{S}_x)_5$ family, and compare the measured phonon frequencies at low temperatures with the calculated values. In Sec. IV from the temperature dependence of the phonon intensity we obtain phase transition temperatures, which are compared with the resistance measurements. In Sec. V we analyze the Fano interference feature of B_{2g} -symmetry Raman response. In Sec. VI we present the temperature dependence of phonon-mode parameters: the results for B_{2g} -symmetry modes are given in SubSec. VIA, and those for A_g -symmetry modes are given in SubSec. VIB. In Sec. VII we convert Raman response from frequency domain to time domain, and discuss relevant time-resolved studies on Ta_2NiSe_5 . In Sec. VIII we provide a summary of the observations and their implications. Further discussion is provided in appendices: the methods used for the estimation of laser heating rate in Appendix. A; the mathematical formalism for the generalized Fano model

in Appendix B, and more illustration of this model in Appendix C; the fitting results of the anharmonic decay model for the phonon modes in Appendix D.

II. EXPERIMENTAL

Single crystals of $\text{Ta}_2\text{Ni}(\text{Se}_{1-x}\text{S}_x)_5$ family were grown by chemical vapor transport method. Elemental powders of tantalum, nickel, selenium and sulfur were mixed with stoichiometric ratio and then sealed in an evacuated quartz ampule with a small amount of iodine as the transport agent. The mixture was placed in the hot end of the ampule ($\sim 950^\circ\text{C}$) under a temperature gradient of about $10^\circ\text{C}/\text{cm}$. After about a week mm-sized needle-like single crystals were found at the cold end of the ampule. The crystals are shiny and cleave easily. We used x-ray diffraction and electron dispersive X-ray spectroscopy to verify the exact composition of the crystals and their uniformity. The samples for resistance and Raman measurements are from the same batch.

The resistance is measured along a axis in a four-probe configuration using a Quantum Design PPMS system.

The TEM images of domain structures are taken on a FEI Titan Themis G2 system using a Gatan double-tilt cryo-stage.

For Raman measurements, the samples were cleaved in ambient conditions to expose the ac plane; the cleaved surfaces were then examined under a Nomarski microscope to find a strain-free area. Raman-scattering measurements were performed in a quasi-back-scattering geometry from the samples mounted in a continuous helium-gas-flow cryostat.

For acquisition of the low frequency Raman response required for this study, we used a custom fast $f/4$ high resolution 500/500/660 mm focal lengths triple-grating spectrometer with 1800mm^{-1} master holographic gratings comprised of (i) aberration corrected subtractive stage providing a reliable 12 orders-of-magnitude stray light rejection at as low frequency as 4cm^{-1} from the elastic line, (ii) a third stage monochromator, and (iii) a liquid-nitrogen-cooled charge-coupled device (CCD) detector (Princeton Instruments). All the acquired data were corrected for the spectral response of the spectrometer. Three slit configurations were used: $100\ \mu\text{m}$ slit width providing 0.19meV spectral resolution; $50\ \mu\text{m}$ slit width rendering 0.10meV spectral resolution; and, for high resolution data, $25\ \mu\text{m}$ slit width rendering 0.06meV spectral resolution.

For polarization optics, a Glan-Taylor polarizing prism (Melles Griot) with a better than 10^{-5} extinction ratio to clean the laser excitation beam and a broad-band 50mm polarizing cube (Karl Lambrecht Corporation) with an extinction ratio better than 1:500 for the analyzer was used. Two polarization configurations were employed to probe excitations in different symmetry channels. The relationship between the scattering geometries and the symmetry channels [22] is given in Table I.

TABLE I. The Raman selection rules in the high-temperature orthorhombic (point group D_{2h}) and low-temperature monoclinic (point group C_{2h}) phases. Upon the reduction of symmetry from D_{2h} to C_{2h} , the A_g and B_{2g} irreducible representations of D_{2h} group merge into the A_g irreducible representation of C_{2h} group.

Scattering Geometry	Symmetry Channel (D_{2h} group)	Symmetry Channel (C_{2h} group)
aa	A_g	A_g
ac	B_{2g}	A_g

The 647nm line from a Kr^+ ion laser was used for excitation. Incident light was focused to an elongated along the slit direction $50 \times 100\ \mu\text{m}^2$ spot. For data taken below 310K , laser power of 8mW was used. To reach temperature above 310K , we kept the environmental temperature at 295K and increased laser power to reach higher sample temperature in the excitation spot. All reported data were corrected for laser heating in two mutually consistent ways [Appendix. A]: (i) by Stokes/anti-Stokes intensity ratio analysis, based on the principle of detailed balance, (ii) by checking laser power that is inducing the phase transition. In addition to that, we performed a thermoconductivity model calculation that suggests a linear scaling of the heating rate with the beam spot size.

The first-principle calculations were performed using DFT within Projector Augmented-Wave (PAW) formalism [25] and Perdew-Burke-Ernzerhof (PBE) parametrized exchange-correlation energy functional [26]. For Ta_2NiSe_5 , we used the implementation of the Quantum ESPRESSO package [27], using the pseudopotentials generated by Dal Corso [28] and with grimme-d3 Van-der-Waals correction [29] included. For Ta_2NiS_5 , the implementation of the Vienna Ab initio Simulation Package (VASP) code [30, 31] was used. The phonon frequencies for both cases were calculated by finite displacement method as implemented in PHONOPY [32]. The initial structures subject to relaxation for Ta_2NiSe_5 and Ta_2NiS_5 have been taken from experiments on the high-temperature orthorhombic phase, Ref.[33] and Ref.[34], respectively.

III. OVERVIEW

In this section we show an overview of the phonon spectra of $\text{Ta}_2\text{Ni}(\text{Se}_{1-x}\text{S}_x)_5$ family, and compare the measured phonon frequencies at low temperatures with the calculated values.

The phonon spectra of $\text{Ta}_2\text{Ni}(\text{Se}_{1-x}\text{S}_x)_5$ family ($x=0, 0.25, 0.67, \text{ and } 1$) are summarized in Fig. 2. For stoichiometric compositions at high temperature, we observe 8 modes in aa geometry and 3 modes in ac geometry, in agreement with the $8A_g$ and $3B_{2g}$ Raman-active phonon modes expected in the high-temperature orthorhombic phase (space group $Cmcm$): the A_g modes appear in

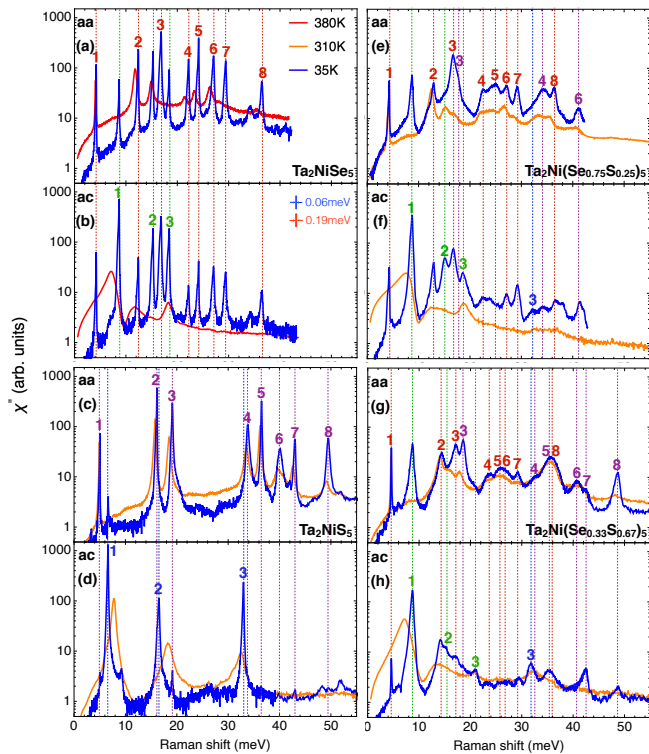


FIG. 2. Raman response χ'' in the aa and ac scattering geometries for $\text{Ta}_2\text{Ni}(\text{Se}_{1-x}\text{S}_x)_5$ family, plotted in semi-log scale. The phonon modes are classified by the A_g and B_{2g} irreducible representations of D_{2h} point group. The A_g and B_{2g} modes of Ta_2NiSe_5 are labeled by red and green colors, respectively; the A_g and B_{2g} modes of Ta_2NiS_5 are labeled by purple and blue colors, respectively. For the samples with $x = 0.25$ and 0.67 , the modes are labeled by the color scheme of Ta_2NiSe_5 if its energy is close to that of Ta_2NiSe_5 modes, or the color scheme of Ta_2NiS_5 if its energy is close to that of Ta_2NiS_5 modes. The spectral resolution is 0.19 meV for the ac spectra at high temperature, and 0.06 meV for the ac spectra at 35 K and all aa spectra.

aa scattering geometry and the B_{2g} modes in ac scattering geometry [Table. I]. Except for the Ta_2NiS_5 sample, the two lowest-energy B_{2g} modes, $B_{2g}^{(1)}$ and $B_{2g}^{(2)}$, exhibit strongly broadened and asymmetric lineshapes at high temperature. This anomalous broadening is almost absent for Ta_2NiS_5 (note the logarithmic intensity scale in Fig. 2).

At low temperature, a transition into a monoclinic phase (space group $C2/c$) occurs. In the low-temperature phase, because of the mirror symmetry breaking, all Raman-active phonon modes appear in both aa and ac scattering geometries [Table. I]. All of the expected Raman-active modes were observed: they are identified by dashed lines in Fig. 2; the additional weak spectral features result from the second-order scattering. For example, the weak feature at 34.1 meV in aa scattering geometry for Ta_2NiSe_5 corresponds to a second-order scattering feature of the 16.8 meV $B_{2g}^{(2)}$ mode.

TABLE II. Comparison of the experimentally measured phonon energies at 35 K and the calculated values for Ta_2NiSe_5 and Ta_2NiS_5 . Unit is meV ; modes are identified by their irreducible representations in the orthorhombic phase, where $8 A_g$ modes and $3 B_{2g}$ modes are expected.

Mode	Ta_2NiSe_5		Ta_2NiS_5	
	Exp.	Calc.	Exp.	Calc.
$A_g^{(1)}$	4.22	4.22	5.01	4.82
$B_{2g}^{(1)}$	8.66	7.61	6.50	7.66
$A_g^{(2)}$	12.28	11.87	16.13	15.18
$B_{2g}^{(2)}$	15.25	10.14	16.41	16.20
$A_g^{(3)}$	16.76	15.53	19.13	18.27
$B_{2g}^{(3)}$	18.38	19.39	32.96	33.23
$A_g^{(4)}$	22.17	21.91	33.82	33.82
$A_g^{(5)}$	24.14	24.09	36.50	36.36
$A_g^{(6)}$	27.02	26.34	40.07	40.13
$A_g^{(7)}$	29.39	29.01	43.10	43.07
$A_g^{(8)}$	36.32	37.47	49.49	49.62

The measured phonon frequencies for Ta_2NiSe_5 and Ta_2NiS_5 at 35 K generally match well with the calculated values [Table. II]. As the calculations were carried out in the orthorhombic phase, this suggests that monoclinicity by itself does not strongly affect the phonon frequencies. Larger than 10% discrepancies between the measured and calculated values appear only for the $B_{2g}^{(1)}$ and $B_{2g}^{(2)}$ modes of Ta_2NiSe_5 and the $B_{2g}^{(1)}$ mode of Ta_2NiS_5 . As discussed in Sec. V, these modes exhibit an anomalous behavior that can be attributed to their strong coupling to the excitons.

For the alloy compositions ($x = 0.25$ and 0.67), the phonon modes show larger linewidth compared with that for the stoichiometric compositions. Moreover, the $B_{2g}^{(3)}$ and $A_g^{(3)}$ - $A_g^{(8)}$ modes exhibit two distinct frequencies: one close to the frequency of that mode in Ta_2NiSe_5 , and the other close to the frequency in Ta_2NiS_5 . Such behavior is commonly observed for alloys in which the frequencies of the same phonon mode in the two end-point materials differ substantially [35–37]. The doping dependence of the phonon frequencies measured at 35 K is presented in Fig. 3. The frequencies of the phonon modes for Ta_2NiSe_5 are consistent with the recent experimental studies [38–42] and the calculated values [43].

IV. PHASE TRANSITION

In this section we deduce the phase transition temperatures from the observed change in selection rules in Raman response and compare the results with the resistance measurements.

Below T_c , the 11 phonon modes are allowed by symmetry to appear in both scattering geometries [Table. I];

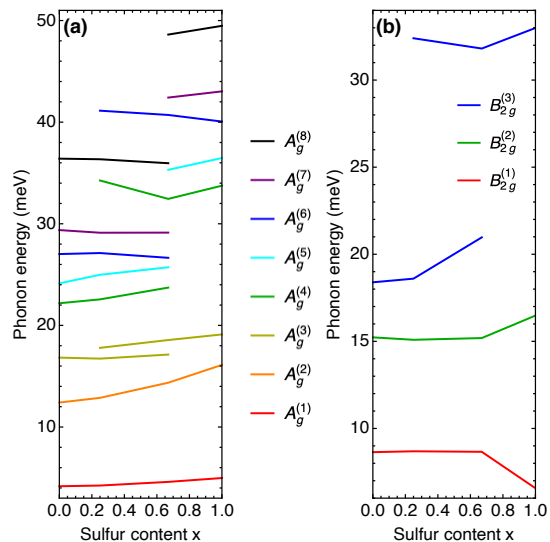


FIG. 3. The doping dependence of the Raman-active phonon frequencies at 35 K for $\text{Ta}_2\text{Ni}(\text{Se}_{1-x}\text{S}_x)_5$ family. For the doped samples, the $B_{2g}^{(3)}$ and $A_g^{(3)}$ - $A_g^{(8)}$ phonons exhibit two-mode behavior (i.e. two peaks in the spectrum), characteristic of alloys [35–37].

thus, 8 additional modes appear in ac geometry and 3 in aa . We call the appearance of phonon modes below T_c in the orthogonal to allowed above T_c scattering geometry as phonon-mode "leakage". As shown in Fig. 2, all four samples exhibit phonon-mode "leakage" at low temperature, indicating presence of a point group symmetry breaking structural phase transition.

In Fig. 4 we show the temperature dependence of the "leakage" of $A_g^{(1)}$ and $B_{2g}^{(1)}$ modes for $\text{Ta}_2\text{Ni}(\text{Se}_{1-x}\text{S}_x)_5$ family. The "leakage" of other modes is given in Sec. VI. For each sample, the "leakage" of different modes appear below the same temperature.

We assign the temperature of the "leakage" onset as

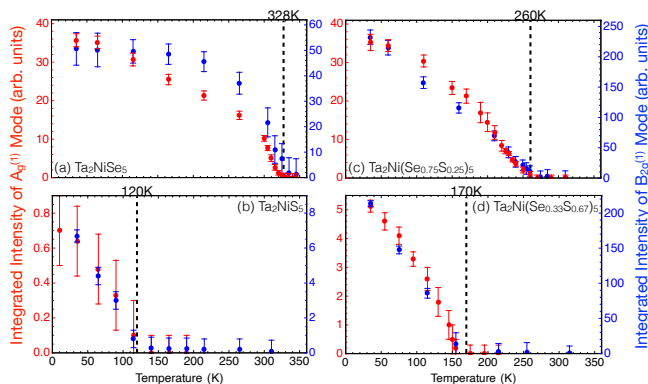


FIG. 4. Temperature dependence of the integrated intensity of $A_g^{(1)}$ and $B_{2g}^{(1)}$ modes in the 'forbidden' scattering geometry (ac and aa , respectively) for (a) Ta_2NiSe_5 , (b) Ta_2NiS_5 , (c) $\text{Ta}_2\text{Ni}(\text{Se}_{0.75}\text{S}_{0.25})_5$, and (d) $\text{Ta}_2\text{Ni}(\text{Se}_{0.33}\text{S}_{0.67})_5$.

TABLE III. The structural phase transition temperature of $\text{Ta}_2\text{Ni}(\text{Se}_{1-x}\text{S}_x)_5$ family determined by observing phonon-mode "leakage" in Raman spectra.

Sulfur Content x	Transition Temp. (K)
0	328 ± 5
0.25	260 ± 10
0.67	170 ± 10
1	120 ± 10

the structural phase transition temperature T_c . The phase transition temperatures for $\text{Ta}_2\text{Ni}(\text{Se}_{1-x}\text{S}_x)_5$ family are given in Table III. The transition temperatures $T_c(x)$ decrease with sulfur doping x . Moreover, for larger sulfur content x the phonon intensities in the 'forbidden' scattering geometry also decrease. This quantity is proportional to the square of the order parameter (OP), which can be represented by, e.g., the deviation of the angle β between a and c axes [Fig. 1 (b)] from 90° . While the general monotonic growth of the leakage intensity on cooling is consistent with these expectations, the details of temperature dependence can vary for different modes [Fig. 4(a)]. The decreasing trend of the phonon intensity in the 'forbidden' scattering geometry with sulfur content x therefore indicates that the structural distortion becomes weaker with higher sulfur concentration.

A complementary way to determine the phase transition temperature was demonstrated in [8], where anomalies in the temperature dependence of resistance have been detected at $T_c(x)$. In Fig. 5 we show the resistance data analysis for the samples from the same batch as used for the Raman measurements. For Ta_2NiSe_5 and $\text{Ta}_2\text{Ni}(\text{Se}_{0.75}\text{S}_{0.25})_5$, the temperature at which the temperature derivative of resistance displays a kink and that of transport activation gap shows a peak, coincides with the Raman-determined transition temperature. For $\text{Ta}_2\text{Ni}(\text{Se}_{0.33}\text{S}_{0.67})_5$ and Ta_2NiS_5 , though, the features in resistance data are less pronounced. The latter can be anticipated from their much more insulating character, potentially masking a small change of resistance due to transition on top of a large background resistance.

V. FANO INTERFERENCE IN THE B_{2g} SYMMETRY CHANNEL

In this section we analyze the asymmetric lineshape of the B_{2g} -symmetry phonon modes observed for $x < 0.7$ in the high temperature phase. We describe the asymmetric lineshape and its temperature dependence in SubSec. V A. To fit the spectra, we develop a generalized Fano model, discussed in SubSec. V B, in which the asymmetric broadening results from the coupling of the phonon modes to an excitonic continuum. Besides the optical phonon modes, the excitonic continuum also couples to the acoustic phonon mode. We discuss how such

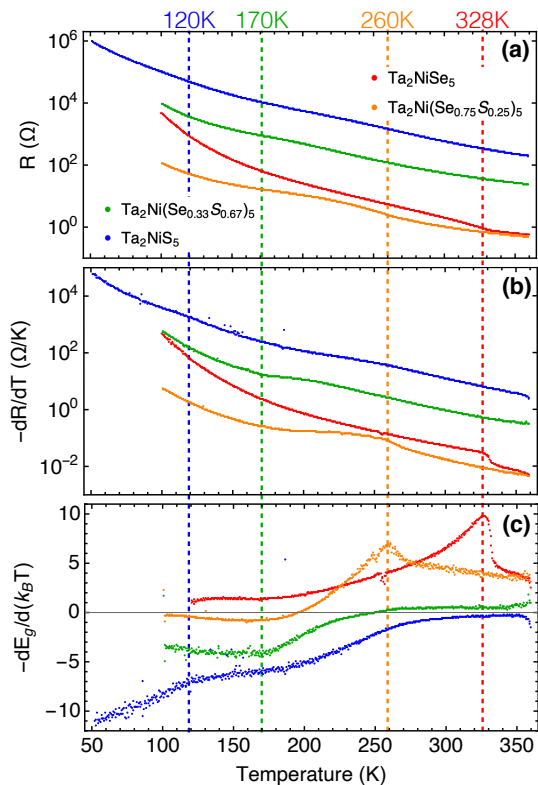


FIG. 5. Temperature dependence of the resistance along a axis for $\text{Ta}_2\text{Ni}(\text{Se}_{1-x}\text{S}_x)_5$ family. (a) The resistance, plotted in semi-log scale. (b) The temperature derivative of resistance, plotted in semi-log scale. (c) The temperature derivative of the transport activation gap $E_g = k_B T \log_{10} [R(T)/R(360\text{K})]$. The transition temperatures determined from Raman measurements are marked by dashed lines for comparison.

coupling enhances the transition temperature $T_c(x)$, and leads to softening of the B_{2g} -symmetry acoustic mode in SubSec. VC. The appearance of a quasi-periodic domain wall structure below T_c introduces additional complexity, and in SubSec. VD, we discuss how the fitting model must be modified to account for low-energy spectral features which are absent above T_c . The fitting results for Ta_2NiSe_5 , relevant to the excitonic continuum, are presented and interpreted in SubSec. VE (those related to the intrinsic phonon properties are shown later in Sec. VI). It is demonstrated that the strengths of the interactions between individual phonons and excitonic continuum are consistent with the displacement patterns deduced from *ab initio* calculations. For comparison, the fitting results for the alloy compositions are given in SubSec. VF.

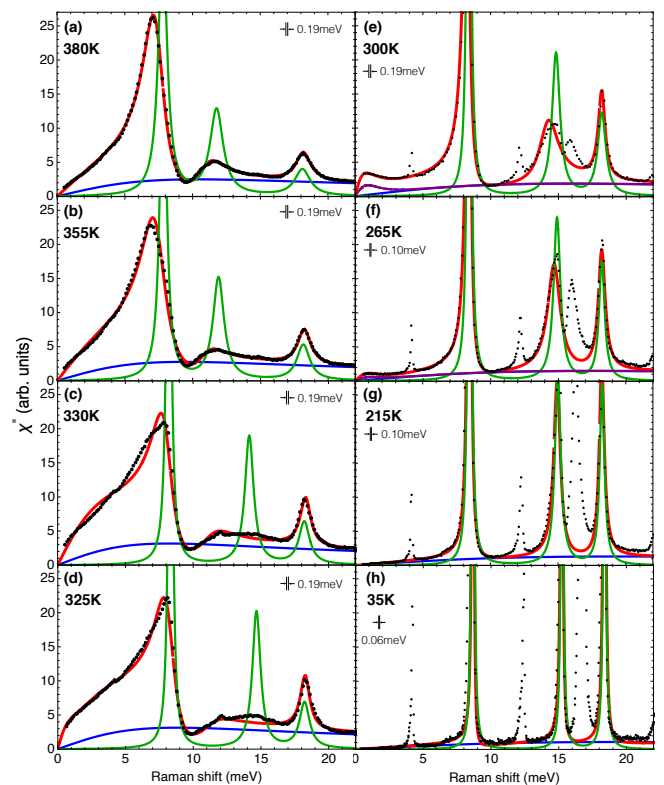


FIG. 6. Temperature dependence of Raman response χ'' in the ac scattering geometry for Ta_2NiSe_5 . The data is shown by black dots, along with the Fano fits [Eq. (B1)] shown as red curves. The spectral resolution is 0.19 meV for panels (a-e), 0.10 meV for panels (f-g), and 0.06 meV for panel (h). The Fano model describes the coupled dynamics of the $B_{2g}^{(1)}\text{-}B_{2g}^{(3)}$ phonon modes and the overdamped excitonic continuum. The bare phonon modes [Eq. (1)] are shown by green curves, and the bare excitonic continuum [Eq. (2)] is shown by blue curves. Below T_c , especially at 300 K, additional spectral weight is observed at low energies, resulting from the emergence of finite-energy acoustic modes due to scattering off structural domain walls (see Fig.9). The purple curves show the coupled response of the acoustic modes and the excitonic continuum. As the excitonic continuum is suppressed on cooling below T_c , the lineshapes of the phonons become essentially symmetric.

A. Temperature dependence of asymmetric Fano lineshapes

The temperature dependence of the spectra measured in ac scattering geometry for Ta_2NiSe_5 is shown in Fig. 6. Above T_c , the $B_{2g}^{(1)}$ and $B_{2g}^{(2)}$ modes have noticeably asymmetric lineshapes, while the lineshape of the $B_{2g}^{(3)}$ mode remains quite symmetric. Upon approaching T_c on cooling, the spectral weight of low-frequency continuum displays an enhancement, and the apparent linewidths of the $B_{2g}^{(1)}$ and $B_{2g}^{(2)}$ modes increase. Below T_c , the modes recover the conventional Lorentzian lineshapes.

An asymmetric lineshape arises due to Fano interfer-

ence when a sharp phonon interacts with a broad continuum. In this case, the continuum is due to the overdamped exciton fluctuations [23, 24], and the exciton-phonon interaction is caused by modulation of electronic bands near the Fermi surface by the B_{2g} -symmetry lattice vibrations.

B. The generalized Fano model for data above T_c

We describe the Fano model that includes the coupling between the $B_{2g}^{(1-3)}$ phonon modes and the continuum; more details can be found in Appendix B.

We first discuss the Raman response of the phonons. The Raman scattering intensity is related to the fluctuation spectrum of the phonon coordinate $\langle Q_\omega Q_{-\omega} \rangle$ [44], which is given by the imaginary part of the phonon coordinate susceptibility $\chi_p''(\omega)$ times the Bose factor. The phononic Raman response function consequently has the form:

$$\chi_p''^{(0)}(\omega) = \frac{4t_p^2\omega\omega_p\gamma_p}{(\omega^2 - \omega_p^2)^2 + 2\gamma_p^2(\omega^2 + \omega_p^2) + \gamma_p^4}, \quad (1)$$

where t_p is the light-scattering vertex for the phonon, ω_p is the mode's bare frequency, and γ_p is the half width at half maximum (HWHM) which is related to the oscillator lifetime.

An exciton in a gapped system (a semiconductor or insulator) is expected to have a sharply peaked response at the exciton energy described by a bosonic response function similar to the Eq. (1). The most important difference for a semimetal is the presence of a gapless continuum of interband particle-hole excitations enabling the decay of the $\mathbf{q} = 0$ exciton into unbound particle-hole pairs (Landau damping). To describe the continuum in data, we find it sufficient to assume a purely relaxational dynamics (corresponding to strong overdamping) for the excitonic response. This leads to the form

$$\chi_e''^{(0)}(\omega) = \frac{t_e^2\omega}{(\omega_e^2/\gamma_e)^2 + \omega^2}, \quad (2)$$

where t_e controls the overall intensity determined by the light-scattering vertex and the excitonic density of states, ω_e is the frequency of the over-damped excitation, and γ_e is the relaxation rate, typically much larger than ω_e . Note that for the purpose of the fitting description below $\Omega_e(T) = \omega_e^2/\gamma_e$ is a single parameter denoting the temperature-dependent peak frequency in the broad response function $\chi_e''(\omega)$. For a purely excitonic transition this peak represents the soft mode: $\Omega_e(T_c^{el}) = 0$ is the condition for bare excitonic transition temperature at T_c^{el} , where the static excitonic susceptibility $\chi_e(0)$ diverges (see Eq. (B20)).

In the absence of the exciton-phonon interaction between the modes the respective phononic and excitonic responses [Eqs.(1) and (2)] simply sum up. The exciton-phonon interaction, however, couples these dynamical responses: in particular, a bilinear coupling of the exciton

and the B_{2g} phonon coordinates is expected [18] (note that the bare phonons are diagonal normal modes and thus no bilinear interaction between them is present). The resulting response can be obtained by solving the coupled equations of motion [Appendix B]. Each of the responses $\chi_p''(\omega)$ and $\chi_e''(\omega)$ get renormalized by the interaction, and in addition, the response of the phonon coordinate to the exciton one, $\chi_{int}''(\omega)$, becomes finite. The latter leads to an essential interference term in the total Raman response function [45–47].

To appreciate the effect of renormalization, we first consider a simplified case in which the excitonic continuum couples to a single sharp phonon mode ($\gamma_p \ll \omega_p$) [Appendix C]. Then, solving the coupled dynamical equations, one obtains the full Raman response function

$$\chi''(\omega) = \frac{\omega[2t_p v \omega_p - t_e(\omega^2 - \omega_p^2)]^2}{(\Omega_e^2 + \omega^2)(\omega^2 - \omega_p^2)^2 + 4\Omega_e v^2 \omega_p (\omega^2 - \omega_p^2) + 4v^4 \omega_p^2} \quad (3)$$

could be broken down into a sum of three contributions:

$$\chi''(\omega) = \chi_p''(\omega) + \chi_e''(\omega) + \chi_{int}''(\omega), \quad (4)$$

where the first two terms correspond to the phonon response proportional to square of light coupling vertex t_p^2 and the excitonic continuum proportional to t_e^2 , respectively, while the third one, that is proportional to the $t_p t_e$ combination, is the interference term appearing due to the exciton-phonon coupling with strength v [47].

We first discuss the phonon response in the presence of the coupling with the excitonic continuum. As we will show now, the coupling to the continuum of overdamped excitonic excitations renormalizes the bare linewidth to

$$\gamma_p^v = \frac{v^2 \omega_p}{\omega_p^2 + \Omega_e^2}, \quad (5)$$

thus, the bare γ_p can be neglected altogether [48] The renormalized phonon response is given by

$$\chi_p''(\omega) = \frac{4t_p^2\omega\omega_p\gamma_p^v}{[\omega^2 - (\omega_p^2 - 2\Omega_e\gamma_p^v)]^2 + 4\omega_p^2\gamma_p^{v2} + \frac{(\omega^2 - \omega_p^2)^3}{\omega_p^2 + \Omega_e^2}}. \quad (6)$$

Comparing Eq.(6) to Eq.(1) for the bare phonon, the phonon frequency renormalization is $\omega_p^2 \rightarrow \omega_p^2 - 2\Omega_e\gamma_p^v$ [49]. On increasing coupling strength v , the phononic response maximum shifts to $\omega_{p,max} = \omega_p - \frac{v^2(2\omega_p\Omega_e - v^2)}{2(v^2\Omega_e + \omega_p\Omega_e^2 + \omega_p^3)}$.

For the excitonic response $\chi_e''(\omega)$ the renormalization effects are most significant. Those are best illustrated by the low-frequency slope of the excitonic response function $\left. \frac{\partial \chi_e''(\omega)}{\partial \omega} \right|_{\omega \rightarrow 0}$. In the absence of exciton-phonon interaction the low frequency slope for the bare response

is equal to t_e^2/Ω_e^2 (see Eq. (2)), while the interaction v is rapidly enhancing the slope as

$$\left. \frac{\partial \chi_e''(\omega)}{\partial \omega} \right|_{\omega \rightarrow 0} = \frac{t_e^2}{\left[\Omega_e(T) - \frac{2v^2}{\omega_p} \right]^2}, \quad (7)$$

leading to a critical value at $v_{cr} = \sqrt{\Omega_e \omega_p / 2}$, when the excitonic spectral weight is pushed to the lowest frequencies and thus causing the divergence in the static susceptibility

$$\chi(\omega \rightarrow 0, T) = \frac{t_e^2 - 4t_e t_p \frac{v}{\omega_p} + 2t_p^2 \frac{\Omega_e(T)}{\omega_p}}{\Omega_e(T) - \frac{2v^2}{\omega_p}}, \quad (8)$$

signifying the enhancement of the excitonic phase transition temperature, caused by coupling to the optical phonon.

Finally, the mutual response of the exciton and phonon coordinates appearing due to the coupling v between them, leads to the sign-changing interference term

$$\chi_{int}''(\omega) = \frac{4t_e t_p v \omega \omega_p \frac{\omega_p^2 - \omega^2}{\Omega_e^2 + \omega_p^2}}{\left[\omega^2 - (\omega_p^2 - 2\Omega_e \gamma_p^v) \right]^2 + 4\omega_p^2 \gamma_p^{v2} + \frac{(\omega^2 - \omega_p^2)^3}{\omega_p^2 + \Omega_e^2}}. \quad (9)$$

The sign of this term depends on phase difference between the exciton and phonon oscillators. Because the phase of driven by light phononic oscillator is flipping to the opposite one at the resonant frequency, the sign of this term changes close to the bare phonon frequency ω_p . Thus, this term is chiefly responsible for a skewed, asymmetric shape of the resulting Fano feature. Depending on the sign of v the peak is skewed to the left or to the right of the original phonon frequency. Note that even for weak coupling $v \ll \omega_p$ this term can have an appreciable magnitude close to the phonon energy.

To analyze the actual measured low-frequency data shown in Fig. 6, we use the model with three B_{2g} optical phonon modes, all interacting with the excitonic continuum, see for details Appendix B. As above, the total Raman response $\chi''(\omega)$ can be similarly decomposed into three contributions, Eq. (4): the first two describing the renormalized phononic and excitonic responses, respectively, with the third one arising due to the interference effects. In Fig. 7, an example of such decomposition is shown for the data taken at 380 K, along with the deduced bare responses (without the effect of coupling), $\chi_p''^{(0)}(\omega)$ and $\chi_e''^{(0)}(\omega)$. The renormalized phonon features become broader due to the interaction with the continuum and their frequencies shift. Most importantly, the coupling noticeably increases the excitonic response at low frequencies. The sign-changing interference term enhances the asymmetric lineshape of the combined response.

To fit the ac spectra, first, we determine the t_e parameter of the excitonic continuum (Eq. (2)) by fitting the phonon free region of spectra between 25 and

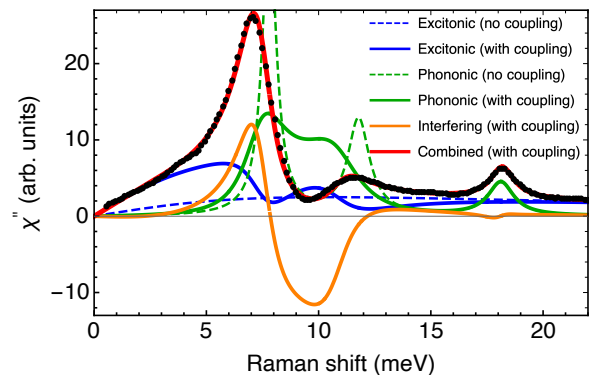


FIG. 7. The effect of coupling on Raman spectrum, relevant to the data measured for Ta_2NiSe_5 at 380 K. The Raman response functions are shown for bare (dashed lines) and renormalized by interaction (solid lines), $\chi_{e,p}''^{(0)}(\omega)$ and $\chi_{e,p}''(\omega)$ correspondingly. The interference term $\chi_{int}''(\omega)$ is shown by solid orange line. The solid red line corresponds to the total sum of the solid blue, solid green, and solid orange lines, Eq. (4). The black dots represent the experimentally measured spectrum.

40 meV. As expected, this quantity remains temperature-independent [Fig. 10(b)]. Second, we perform a global fitting of the spectral region below 22 meV for all measured temperatures. We assume (consistently with the expectation due to anharmonic effects, see Eq. (16-17) below) the linewidth of the three B_{2g} -symmetry phonon modes to be a linear function of temperature above T_c . For spectra below T_c , we fit the "leaked" phonon modes with the Lorentzian lineshapes, and account for their contribution in the global fitting.

C. The coupling between excitonic continuum and acoustic modes

Besides the optical phonon modes, the excitonic continuum also couples to the acoustic phonon modes. The acoustic branch has a linear dispersion $\omega_s(q) = c_s q$ (c_s is sound velocity) at small wavenectors q ; its coupling to light and to the excitonic continuum both vanish in the long-wavelength limit [50]: $t_s = \tau_s \sqrt{q}$ and $v_s = \beta_s \sqrt{q}$ (τ_s and β_s are constants). However, the acoustic mode has important contribution to the enhancement of the phase-transition temperature [51]. The diverging condition for static Raman susceptibility $\chi(\omega \rightarrow 0, T)$ is defined by coupling to all modes, optical and acoustic:

$$\tilde{\Omega}_e(T_c) - \frac{2\beta_s^2}{c_s} = 0, \quad (10)$$

in which

$$\tilde{\Omega}_e(T) = \Omega_e(T) - \sum_{i=1}^3 \frac{2v_i^2}{\omega_{pi}}. \quad (11)$$

This equation determines the symmetry-breaking phase transition temperature T_c .

Because the spectroscopic Fano feature associated with the coupling between the long-wavelength longitudinal acoustic mode and the excitonic continuum lies at frequencies far below accessibility of Raman experiment, the constant β_s cannot be derived directly from an interference feature of a typical Raman spectra. Nevertheless, the coupling constant β_s has observable consequences already above T_c . In particular, the acoustic mode has been shown to soften on cooling towards T_c [52]. This softening does not result from intrinsic instability of the acoustic modes; rather, it is caused by the coupling of the acoustic mode to the softening excitonic excitations [Eq. (2)].

To demonstrate this point, we solve for the lowest-energy pole of the Green's function for the interacting phononic and excitonic excitations assuming an infinitesimal q . The energy of the pole gives the renormalized (experimentally-measured) sound velocity \tilde{c}_s above T_c [Eq. (B23) of Appendix B]:

$$\tilde{c}_s^2 = c_s^2 - \frac{2\beta_s^2 c_s}{\tilde{\Omega}_e(T)}, \quad (12)$$

in which c_s is the bare sound velocity in the absence of coupling to the excitons. Eq. (10) enables us to rewrite Eq. (12) as

$$\tilde{c}_s(T) = c_s \sqrt{1 - \frac{\tilde{\Omega}_e(T_c)}{\tilde{\Omega}_e(T)}}. \quad (13)$$

From Eq. (13), it is clear that the sound velocity softens to zero at T_c in the absence of any intrinsic ferroelastic instability. The renormalization of the sound velocity above T_c can be estimated by using Eq. (13). Using the low-temperature value of the sound velocity c_s [52], we can then calculate $\tilde{c}_s(T)$ with the parameters obtained from the Fano fits, i.e. without free parameters. The result yields $\tilde{c}_s(T = 400\text{K})/c_s \approx 0.65$, which is in remarkable agreement with the experimental ratio $\tilde{c}_{s,exp}(T = 400\text{K})/c_{s,exp} \approx 0.65$. The agreement between the estimated and experimentally-determined values suggests that in Ta_2NiSe_5 , the softening of the acoustic mode results solely from the coupling to the softening excitonic excitations.

D. The generalized Fano model for data below T_c

Below T_c , especially around 300 K, this model appears to be insufficient to account for an additional low-frequency spectral weight, see Fig. 6(e) and Fig. 8. To understand the origin of this spectral feature below a few meV, we recall that below T_c formation of quasi-periodic structural domains have been observed by transmission electron microscopy (TEM) [9, 15]. Such quasi-periodic structure can take a recoil of quasi-momenta, enabling Raman coupling to acoustic mode at finite momentum $q_d = \frac{2\pi}{d}$, where d is the periodicity of the domain

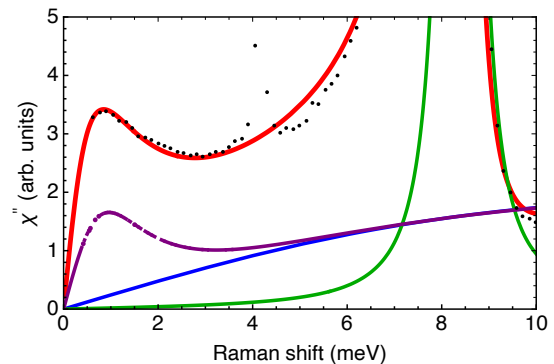


FIG. 8. The contribution from the acoustic modes to low-frequency Raman spectrum in *ac* polarization, relevant to the data measured for Ta_2NiSe_5 at 300 K. The data is shown by black dots; the total Fano fit is shown as red curve; the bare excitonic and phononic components are presented in blue and green, respectively; the coupled response of the acoustic and excitonic components is shown in purple.

pattern, causing the appearance of the additional spectral feature at frequency $\omega_d \approx c_s q_d$. Therefore, fitting this ultra-low-frequency spectral feature provides an independent approach to determine the coupling constant $v_d = \beta_s \sqrt{q_d}$ between the acoustic lattice excitations and the excitonic continuum, and hence define the constant β_s that controls the enhancement of the transition temperature to T_c due to coupling between excitons and longitudinal strain fields of the same symmetry. This low-energy feature due to recoil on the quasi-periodic structure of domain walls is best seen about 30 K below T_c , when the excitonic continuum is sufficiently suppressed but still adequate to provide a Fano-interference feature.

In Fig. 9 we compare two TEM images from *ac* plane of Ta_2NiSe_5 measured above and below T_c . The domains have stripe shape, aligned parallel to the *a*-axis. The average spacing \bar{d} between these stripes along *c*-axis direction is on the order of 200 Å. For the purpose of spectral analysis, we will assume that the spacing between stripes i in units of the crystal unit cell constant c follows the Poisson distribution

$$P(i; \mu = \frac{\bar{d}}{c}) = \frac{\mu^i e^{-\mu}}{i!}, \quad (14)$$

where μ is average inter-domain distance in the number of *c*-direction unit cells.

We deduce the unrenormalized speed of sound from the dispersion of the acoustic mode measured by inelastic x-ray scattering at temperatures far away from T_c : $c_s \approx 30 \text{ meV \AA}$, see Ref. [52]. We also note that at high temperatures the acoustic excitations away from long-wavelength limit are significantly broadened [52].

Recognizing that the low-frequency feature is inhomogeneously broadened by random distribution of the stripe distances, for the fitting procedure to the measured response function we perform summation over the distri-

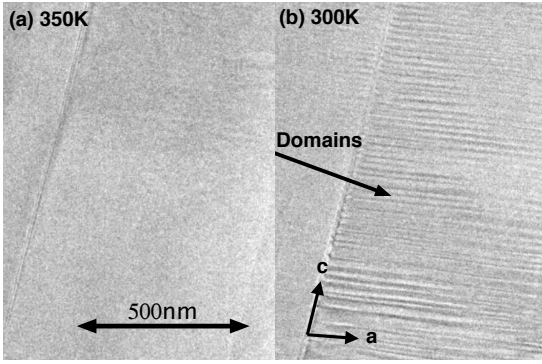


FIG. 9. Two images of the Ta_2NiSe_5 recorded from the ac plane by transmission electron microscopy at (a) 350 K and (b) 300 K.

bution function:

$$\chi''(\omega) = \sum_{i=1}^{\infty} P(i; \mu) \chi_i''(\omega), \quad (15)$$

in which each $\chi_i''(\omega)$ is the full response function containing coupling to acoustic mode for domain walls i lattice constants apart, see Eq. (B17) in Appendix. As a reminder, for each individual component, the frequency and HWHM are proportional to q_i ; the light-scattering vertex and coupling are proportional to $\sqrt{q_i}$.

E. The fitting results for Ta_2NiSe_5

The fits to the data, as well as the phononic and excitonic components, are shown in Fig. 6. For the 300 K and 265 K spectra below T_c we also include the acoustic contribution due to coupling via quasi-periodic structure of domain walls. In Fig. 8 we show the acoustic contribution at 300 K. The coupling of the excitonic continuum to the acoustic components enhances the low-energy response. The parameter $\beta = 7.7 \text{ meV } \text{\AA}^{\frac{1}{2}}$ is consistent with Eq. (10) for T_c .

The spectral parameters: frequency, FWHM and integrated intensity, – of the three B_{2g} phonon modes are shown in SubSection. VIB. The rest of the fitting parameters are given in Fig. 10.

The temperature dependence of the coupling strength between the individual phonon modes and the excitonic continuum are detailed in Fig. 10(a). The ratios of the coupling strength to the phonon frequency for the $B_{2g}^{(1)}$ and $B_{2g}^{(2)}$ modes above T_c are 0.32 and -0.34, respectively. These ratios are an order of magnitude larger than the typical values for stable systems with similar phonon frequency [47, 53, 54]. On the contrary, the exciton-phonon interaction with the $B_{2g}^{(3)}$ mode is weak. The signs of the coupling for the $B_{2g}^{(1)}$ and $B_{2g}^{(2)}$ modes are opposite. For these two modes, the magnitude of coupling is temperature independent above T_c , but decreases and saturates

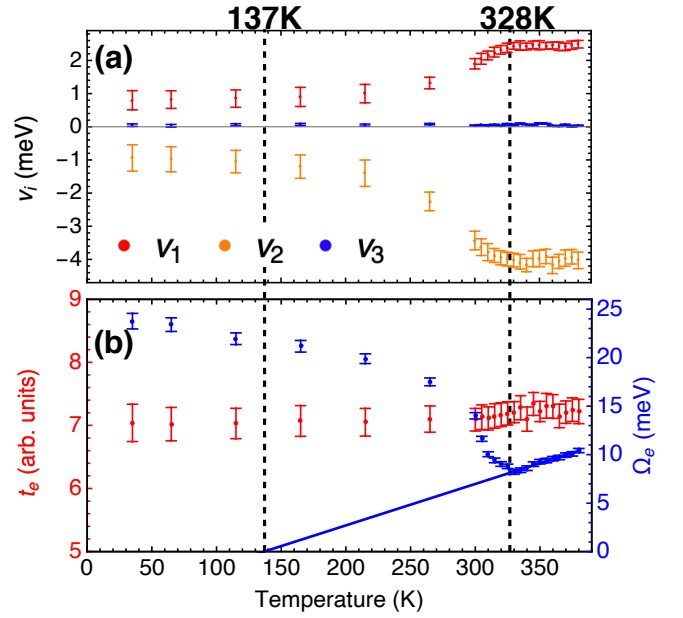


FIG. 10. Temperature dependence of the Fano fitting parameters for the ac Raman spectra of Ta_2NiSe_5 . (a) The coupling strength v_i ($i=1,2,3$) in Eq. (B4). (b) The light-scattering vertex t_e , and the frequency at which the excitonic continuum has maximum intensity $\Omega_e(T) = \omega_c^2/\gamma_e$, Eq. (2). The blue line is a linear fit to the $\Omega_e(T)$ data above T_c . The dashed lines indicate transition temperature T_c and bare excitonic transition temperature T_c^{ex} .

on cooling below T_c . The temperature dependence of the coupling strength is influenced mainly by two factors: the screening effect of free carriers, reduced below T_c due to the emergence of a pronounced spectral gap [23, 55], and the change of the crystal structure below T_c .

The difference in magnitude of the exciton-phonon coupling for $B_{2g}^{(1,2)}$ and $B_{2g}^{(3)}$ modes can be readily understood from the corresponding displacement patterns obtained from the DFT calculations for Ta_2NiSe_5 and shown in Fig. 11. The calculated patterns are consistent with those reported in other studies [20, 52]. While both the $B_{2g}^{(1,2)}$ modes involve displacements of Ta and Se, the $B_{2g}^{(3)}$ mode involve a displacement of Se almost exclusively (the Ni atoms are at the inversion centers and thus do not contribute to the Raman-active phonon modes). As the electronic bands in Ta_2NiSe_5 close to the Fermi level are believed to be predominantly formed by Ta and Ni elec-

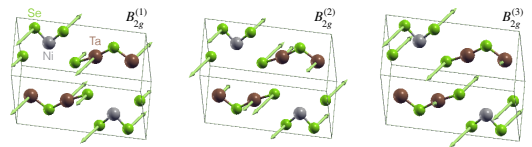


FIG. 11. The calculated vibrational patterns corresponding to the three B_{2g} -symmetry phonon modes of Ta_2NiSe_5 .

trons [12, 18, 19], with much smaller contribution of Se, it appears natural that the $B_{2g}^{(3)}$ mode does not couple to the low-energy electronic degrees of freedom. Furthermore, the vibration of the Ta atoms for $B_{2g}^{(1)}$ and $B_{2g}^{(2)}$ displacements are in anti-phase, which can explain the opposite signs of the exciton-phonon coupling for these modes.

The temperature dependence of the light-scattering vertex t_e and the frequency Ω_e at which the continuum has maximum intensity are shown in Fig. 10(b). Above T_c , the quantity Ω_e linearly decreases on cooling; below T_c , it rapidly increases and saturates at low temperature.

F. The fitting results for $\text{Ta}_2\text{Ni}(\text{Se}_{1-x}\text{S}_x)_5$ with $x = 0.25$ and 0.67

To compare with the results for Ta_2NiSe_5 , we also fit the *ac* polarization spectra for the alloy compositions ($x = 0.25$ and 0.67) above their transition temperature. We are not able to perform a Fano analysis below T_c for two reasons: (a) we have no knowledge of the domain structure and the sound velocity; and (b) we cannot properly subtract the leakage of the A_g modes. In Fig. 12 we show one characteristic Fano fit for $\text{Ta}_2\text{Ni}(\text{Se}_{0.75}\text{S}_{0.25})_5$ and $\text{Ta}_2\text{Ni}(\text{Se}_{0.33}\text{S}_{0.67})_5$, respectively. The fitting parameters are given in Fig. 13.

The results are similar to the case of Ta_2NiSe_5 : for the coupling strength, we find positive v_1 , negative v_2 , and negligible v_3 ; the light-scattering vertex t_e has no temperature dependence above the transition temperature; the energy at which the excitonic continuum has maxi-

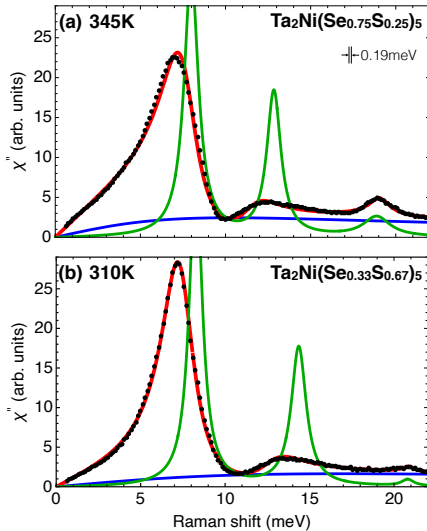


FIG. 12. Raman response χ'' , represented by black dots, in the *ac* scattering geometry for $\text{Ta}_2\text{Ni}(\text{Se}_{0.75}\text{S}_{0.25})_5$ and $\text{Ta}_2\text{Ni}(\text{Se}_{0.33}\text{S}_{0.67})_5$ with the Fano fits [Eq. (B2)] shown as red curves. The spectral resolution is 0.19 meV. The phonon modes [Eq. (1)] and excitonic continuum [Eq. (2)] are represented by green and blue curves, respectively.

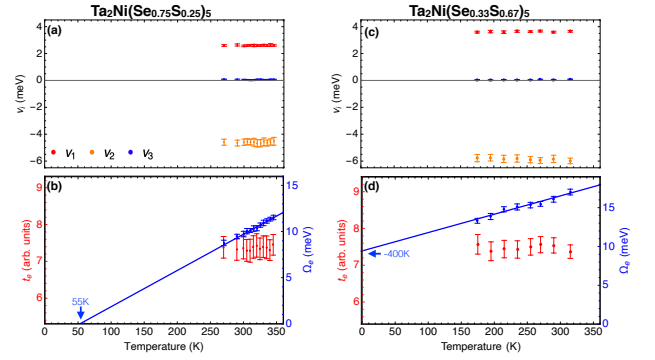


FIG. 13. Temperature dependence of the Fano fitting parameters for the *ac* Raman spectra of $\text{Ta}_2\text{Ni}(\text{Se}_{0.75}\text{S}_{0.25})_5$ (a-b) and $\text{Ta}_2\text{Ni}(\text{Se}_{0.33}\text{S}_{0.67})_5$ (c-d). (a,c) The coupling strength v_i ($i=1,2,3$) in Eq. (B4). (b,d) the light-scattering vertex t_e , and the energy at which the excitonic continuum has maximum intensity $\Omega_e = \omega_e^2/\gamma_e$ of the overdamped electronic mode, Eq. (B6). The blue line is a linear fit to the Ω_e data.

imum intensity, $\Omega_e = \omega_e^2/\gamma_e$, decreases linearly on cooling above the transition temperature. Extrapolating to zero value of Ω_e , we obtain 55 ± 18 K for $\text{Ta}_2\text{Ni}(\text{Se}_{0.75}\text{S}_{0.25})_5$ and -400 ± 70 K for $\text{Ta}_2\text{Ni}(\text{Se}_{0.33}\text{S}_{0.67})_5$.

In Table IV we present the doping dependence of the relevant physical quantities above the transition temperature for $\text{Ta}_2\text{Ni}(\text{Se}_{1-x}\text{S}_x)_5$ family. Because the coupling strength increases with sulfur doping, determining the intrinsic phonon parameters, especially the linewidth, becomes more difficult for $\text{Ta}_2\text{Ni}(\text{Se}_{0.75}\text{S}_{0.25})_5$ and $\text{Ta}_2\text{Ni}(\text{Se}_{0.33}\text{S}_{0.67})_5$.

VI. TEMPERATURE DEPENDENCE OF THE INTRINSIC PHONON PARAMETERS

In this section we present the temperature dependence of intrinsic phonon-mode parameters: energies, intensities and linewidths. The results for B_{2g} -symmetry modes are given in SubSec. VIA, and those for A_g -symmetry modes are given in SubSec. VIB.

TABLE IV. The doping dependence of the scattering vertex and the coupling above the transition temperature for the interaction between the excitonic continuum and phonon modes in the B_{2g} scattering geometry of $\text{Ta}_2\text{Ni}(\text{Se}_{1-x}\text{S}_x)_5$ family. The quantities t_e is the vertex of light scattering process for the excitonic continuum. The quantities v_i ($i=1,2$) are the coupling between the excitonic continuum and the $B_{2g}^{(i)}$ phonon mode.

	$x=0$	$x=0.25$	$x=0.67$
t_e (arb. units)	7.22	7.36	7.48
v_1 (meV)	2.45	2.61	3.61
v_2 (meV)	-4.03	-4.61	-5.87

A. B_{2g} -symmetry Phonon Modes

1. Ta_2NiSe_5

In Fig. 14 we show the temperature dependence of the spectral parameters for B_{2g} -symmetry phonon modes in Ta_2NiSe_5 : the bare phonon frequency, FWHM, and integrated intensity.

Below T_c , the temperature dependence of both frequency $\omega_p(T)$ and FWHM $\Gamma_p(T) = 2\gamma_p(T)$ of the phonon modes can be accounted for by standard model assuming anharmonic decay into two phonons with identical frequencies and opposite momenta [56]:

$$\omega_p(T) = \omega_0 - \omega_2 \left[1 + \frac{2}{e^{\hbar\omega_0/2k_B T} - 1} \right], \quad (16)$$

and

$$\Gamma_p(T) = \Gamma_0 + \Gamma_2 \left[1 + \frac{2}{e^{\hbar\omega_0/2k_B T} - 1} \right]. \quad (17)$$

We note that a low value of Γ_0 indicated high quality of the crystals.

Above T_c , however, the slope of the FWHM increases for the three phonon modes, and the FWHM becomes larger than the value predicted by the anharmonic decay model. The appearance of additional decay channels above T_c is related to the presence of gapless particle-hole pairs. Indeed, above T_c Ta_2NiSe_5 is gapless spectroscopically[23], while below T_c a gap rapidly develops at low energies, suppressing the damping due to particle-hole pairs. Because the Fano model used for fitting takes into account the damping due to exciton-phonon interaction, existence of additional damping

above T_c suggests the importance of the interactions beyond that model, i.e. nonlinear ones.

More noticeable is that the frequencies of the $B_{2g}^{(1)}$ and $B_{2g}^{(2)}$ modes exhibit a large increase on cooling from around 350 K to T_c . The frequency of the $B_{2g}^{(3)}$ mode, however, does not show such anomaly. Only $B_{2g}^{(1)}$ and $B_{2g}^{(2)}$ modes exhibit this anomaly; interestingly (1) they are allowed to couple to interband scattering by symmetry selection rules and (2) their corresponding vibration involve motion of Ni atoms and hence they couple to the electronic bands near Fermi level. Although $B_{2g}^{(3)}$ mode can also couple to the interband scattering, its vibrational pattern almost does not contain motion of Ni atoms.

As for the integrated intensity, $B_{2g}^{(1)}$ and $B_{2g}^{(3)}$ modes have around 2-fold increase of intensity on cooling below T_c , while $B_{2g}^{(2)}$ mode shows temperature-independent intensity. Two factors could influence the intensity. First, the interaction-induced gap opening up below T_c should play a major role. The system gradually changes from a semimetal at high temperature to an insulator at low temperature. The screening effect, which reduces the light-scattering vertex, and in turn, the intensity for phonon modes, is suppressed on cooling. This factor therefore favors increase of intensity on cooling. Second, the structural change below T_c could play also a role. The ion positions are shifted within the unit cell below T_c , and the vibrational patterns of the three B_{2g} modes are modified. Therefore, the polarizability induced by lattice vibrations, which is proportional to the phonon intensity, also change with temperature. The fact that $B_{2g}^{(2)}$ mode shows temperature-independent intensity might be related to its unique vibrational pattern.

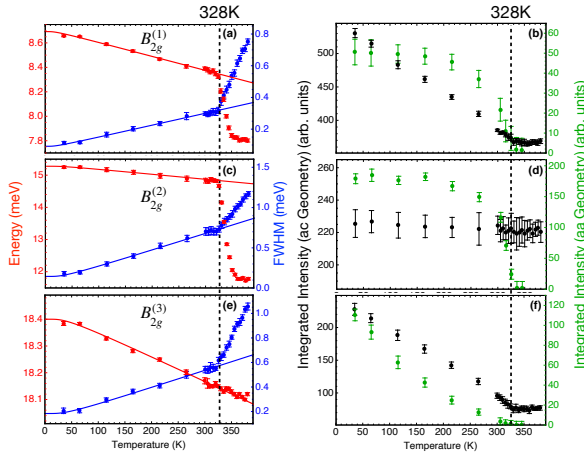


FIG. 14. Temperature dependence of the spectral parameters: the bare frequency, FWHM, and the integrated intensity, – for the B_{2g} -symmetry phonon modes of Ta_2NiSe_5 . For each mode, the left panel presents the frequency and FWHM; and the right panel presents the integrated intensity in the allowed and ‘forbidden’ scattering geometries. The solid lines represent the fits to the anharmonic decay model [Eqs. (16-17)].

2. The alloy compositions ($x=0.25, 0.67$)

In Fig. 15 and 16 we show the temperature dependence of the B_{2g} -mode spectral parameters for $Ta_2Ni(Se_{0.75}S_{0.25})_5$ and $Ta_2Ni(Se_{0.33}S_{0.67})_5$, respectively. Although we do not perform Fano analysis for the data below T_c , we use Lorentzian lineshape to fit the $B_{2g}^{(1)}$ mode at low-enough temperatures, at which the lineshape is essentially symmetric. For the $B_{2g}^{(2)}$ and $B_{2g}^{(3)}$ modes, because they are not well separated from the leakage of A_g modes, it is difficult to reliably obtain their spectral parameters.

For the alloy compositions, the increase of the FWHM slope above T_c is not as strong as in the case of Ta_2NiSe_5 . Moreover, although for Ta_2NiSe_5 the large frequency increase of the $B_{2g}^{(1)}$ mode on cooling happens in a 20 K energy range, the frequency increase for the alloy compositions happens in a much larger energy range.

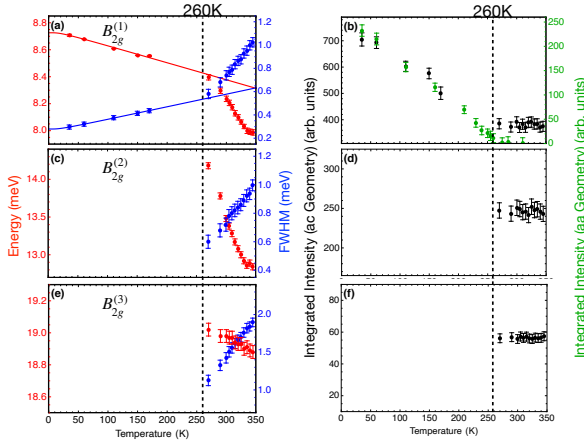


FIG. 15. Temperature dependence of the spectral parameters: frequency, FWHM, and integrated intensity, – for the B_{2g} -symmetry phonon modes of $\text{Ta}_2\text{Ni}(\text{Se}_{0.75}\text{S}_{0.25})_5$. For each mode, the left panel presents the energy and FWHM; the right panel presents the integrated intensity in the allowed and ‘forbidden’ scattering geometries.

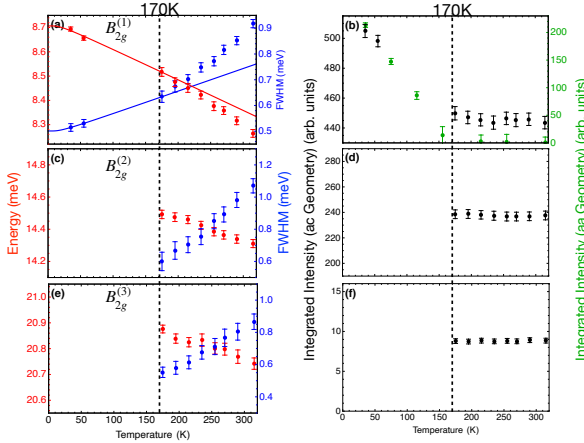


FIG. 16. Temperature dependence of the spectral parameters: frequency, FWHM, and integrated intensity, – for the B_{2g} -symmetry phonon modes of $\text{Ta}_2\text{Ni}(\text{Se}_{0.33}\text{S}_{0.67})_5$. For each mode, the left panel presents the energy and FWHM; the right panel presents the integrated intensity in the allowed and ‘forbidden’ scattering geometries.

3. Ta_2NiS_5

Ta_2NiS_5 is a semiconductor that, in contrast to Ta_2NiSe_5 , does not show signatures of an excitonic insulator like the flattening of valence band dispersion [21, 57]. Consistent with its semiconductor nature, we observe no excitonic continuum and in turn no asymmetric lineshape for the phonon modes, Fig. 2(c-d). In Fig. 17 we zoom in on the temperature dependence of the phonons in *ac* scattering geometry. The three B_{2g} -symmetry phonon modes exhibit conventional Lorentzian lineshapes, and the linewidth has almost 4-fold decrease on cooling from 315 K to 35 K. Moreover, the $B_{2g}^{(1)}$ and

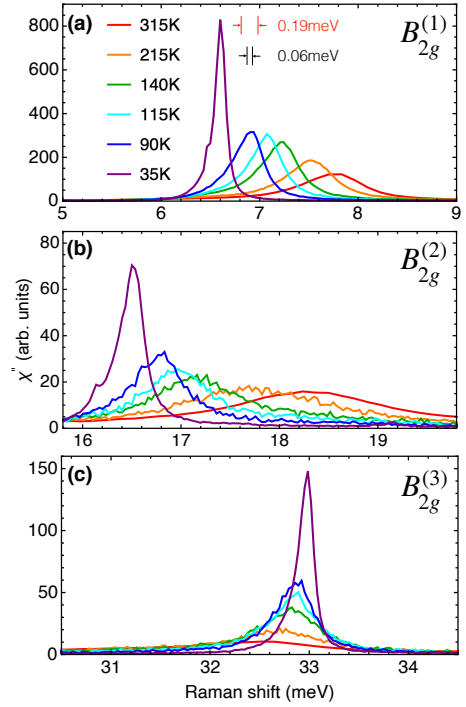


FIG. 17. Temperature dependence of B_{2g} phonons in the *ac* scattering geometry for Ta_2NiS_5 . The spectral resolution is 0.19 meV for the 315 K data, and 0.06 meV for the other data.

$B_{2g}^{(2)}$ modes show softening behavior on cooling.

In Fig. 18 we show the temperature dependence of the spectral parameters for the B_{2g} -symmetry phonon modes for Ta_2NiS_5 : the frequency, FWHM, and the integrated intensity. These spectral parameters are obtained by fitting the measured spectral features with Lorentzian lineshapes.

The behavior of the B_{2g} -symmetry modes is not consistent with the anharmonic decay model: for $B_{2g}^{(1)}$ and $B_{2g}^{(2)}$ modes, the frequency anomalously decreases on cooling; for $B_{2g}^{(3)}$ mode, the decrease of FWHM on cooling is too steep to be accounted by the anharmonic decay model. Hence, we suggest that there is a change in the phonon self energy, which must affect the the apparent mode frequency. For the $B_{2g}^{(1)}$ and $B_{2g}^{(2)}$ modes, whose frequency is below 30 meV, the energy decreases on cooling; for the $B_{2g}^{(3)}$ mode, whose frequency is above 30 meV, the energy increases on cooling.

The integrated intensity of $B_{2g}^{(2)}$ mode is temperature-independent, while that of the other modes increases on cooling. However, different from the case of Ta_2NiSe_5 , in which the increase of the intensity happens below T_c , the intensity increase of the Ta_2NiS_5 modes is through the whole measured temperature range.

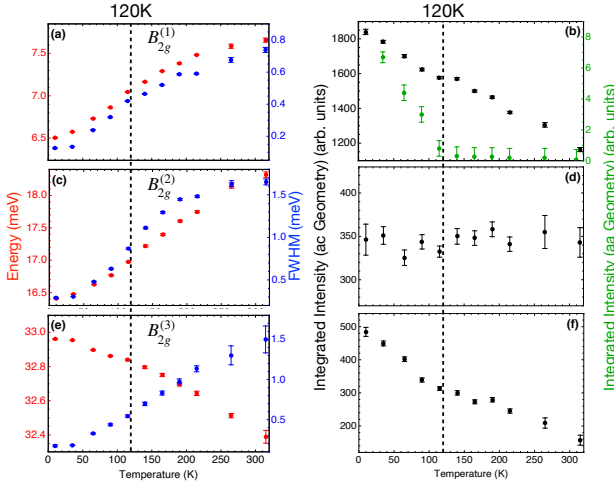


FIG. 18. Temperature dependence of the spectral parameters: frequency, FWHM, and integrated intensity, – for the B_{2g} -symmetry phonon modes of Ta_2NiSe_5 . For each mode, the left panel presents the energy and FWHM; the right panel presents the integrated intensity in the allowed and ‘forbidden’ scattering geometries.

B. A_g -symmetry phonon modes

In this subsection we discuss the properties of the full-symmetric phonon modes; the relevant results are shown in Fig. 19 with respect to the overall spectral weight distribution in the A_g channel, and in Figs. 20 and 21 regarding the spectral parameters of the individual A_g modes. In Fig. 21 we compare the temperature dependence of the spectral parameters (frequency, FWHM, and integrated intensity) of the A_g -symmetry phonon modes for Ta_2NiSe_5 and Ta_2NiS_5 crystals. The temperature dependence of both frequency and FWHM above T_c for these modes can be accounted by the anharmonic decay model [Eq. (16-17)].

The FWHM of the A_g -symmetry modes (except for $A_g^{(3)}$ and $A_g^{(8)}$) for Ta_2NiSe_5 exhibit an anomalous increase above the transition temperature, which we attribute to enhanced electron-phonon scattering rate in its semimetal phase. However, the modes of Ta_2NiS_5 show no anomaly of FWHM, because it is a semiconductor with a direct gap observed throughout the measured temperature range.

The intensity of most modes has more than 2-fold increase on cooling, with a few exceptions: for Ta_2NiSe_5 , the intensity of the $A_g^{(1)}$ mode is independent of temperature, while the intensity of the $A_g^{(2)}$ phonon mode decreases on cooling; for Ta_2NiS_5 , the intensities of the $A_g^{(1)}$ and $A_g^{(2)}$ modes are temperature independent.

The enhancement of intensity on cooling in the semimetallic samples could in principle be related to the change of electronic structure (less screening effect) below T_c . However, an interesting insight can be further obtained by computing the integral $I_{aa}(\omega) = \int_0^\omega \frac{\chi''_{aa}(\omega')}{\omega'} d\omega'$

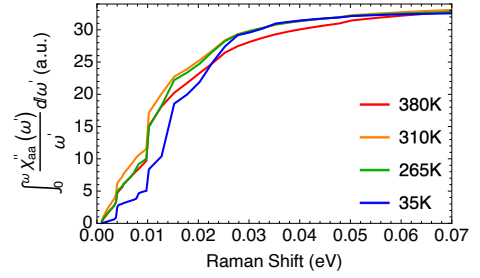


FIG. 19. The integral $I_{aa}(\omega) = \int_0^\omega \frac{\chi''_{aa}(\omega')}{\omega'} d\omega'$ as a function of the Raman shift ω for Ta_2NiSe_5 in aa scattering geometry.

(Fig. 19). In the limit $\omega \rightarrow \infty$ this integral is proportional to the static susceptibility in the aa scattering geometry, which is expected to be approximately constant as a function of temperature since there is no instability in A_g channel. On cooling, the phonon intensity is enhanced [Fig. 21], while the electronic continuum is suppressed [Fig. 2(a)]. However, the integral I_{aa} is essentially temperature independent at 70 meV. This conservation implies that the enhancement of the phonon intensity is balanced by the reduction of the electronic intensity. Note that these effects occur at temperatures below T_c , where the continuum in B_{2g} symmetry is strongly suppressed, indicating the opening of a gap. On the other hand, strong correlation effects have been shown to lead to a non-zero intensity within the gap [23]. Thus, the peculiar balance between the electronic and phononic contributions at low energies implies an unconventional coupling of the electronic modes to the A_g phonons in the correlated excitonic insulator state.

For comparison, in Fig. 20 we show the temperature dependence of the spectral parameters for the $A_g^{(1)}$ mode for $\text{Ta}_2\text{Ni}(\text{Se}_{1-x}\text{S}_x)_5$ with $x = 0.25$ and 0.67 . Because of the difficulty caused by broad lineshape and two-frequency behavior of the phonon modes for alloy compositions, only the lowest-frequency $A_g^{(1)}$ mode, which are well sep-

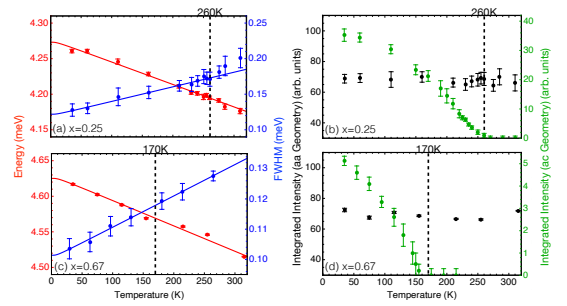


FIG. 20. Temperature dependence of the spectral parameters: frequency, FWHM, and integrated intensity, – for the $A_g^{(1)}$ phonon mode of $\text{Ta}_2\text{Ni}(\text{Se}_{1-x}\text{S}_x)_5$ with $x = 0.25$ (a-b) and 0.67 (c-d). For each sample, the left panel presents the energy and FWHM; the right panel presents the integrated intensity. The solid lines represent the fits to the anharmonic decay model [Eqs. (16-17)].

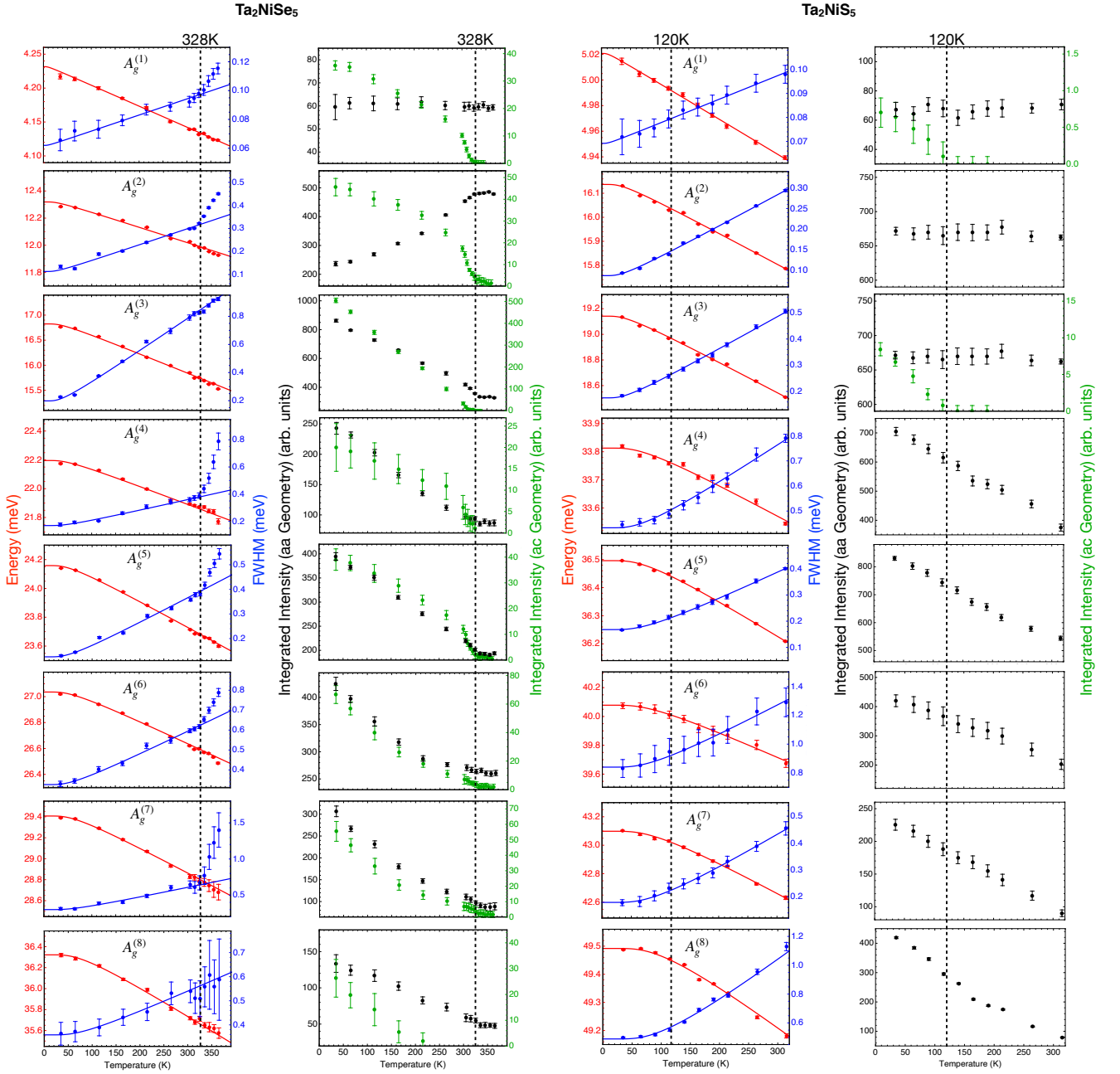


FIG. 21. Temperature dependence of the spectral parameters: frequency, FWHM, and integrated intensity, – for the A_g -symmetry phonon modes for Ta_2NiSe_5 and Ta_2NiS_5 . For each mode, the left panel presents the energy and FWHM; the right panel presents the integrated intensity. The solid lines represent the fits to the anharmonic decay model [Eqs. (16-17)].

arated from other modes in frequency, renders reliable fitting results. For $\text{Ta}_2\text{Ni}(\text{Se}_{0.75}\text{S}_{0.25})_5$, some linewidth broadening is observed above T_c , which is weaker than for Ta_2NiSe_5 . However, for $\text{Ta}_2\text{Ni}(\text{Se}_{0.33}\text{S}_{0.67})_5$ almost no broadening is observed.

VII. RELATION TO TIME-RESOLVED EXPERIMENTS

In this section we convert Raman response from frequency domain to time domain, and discuss relevant time-resolved studies on Ta_2NiSe_5 .

We first discuss the appearance of B_{2g} -symmetry excitations in the time domain, obtained by inverse Fourier transform of the Raman response, see Fig. 22. Above the

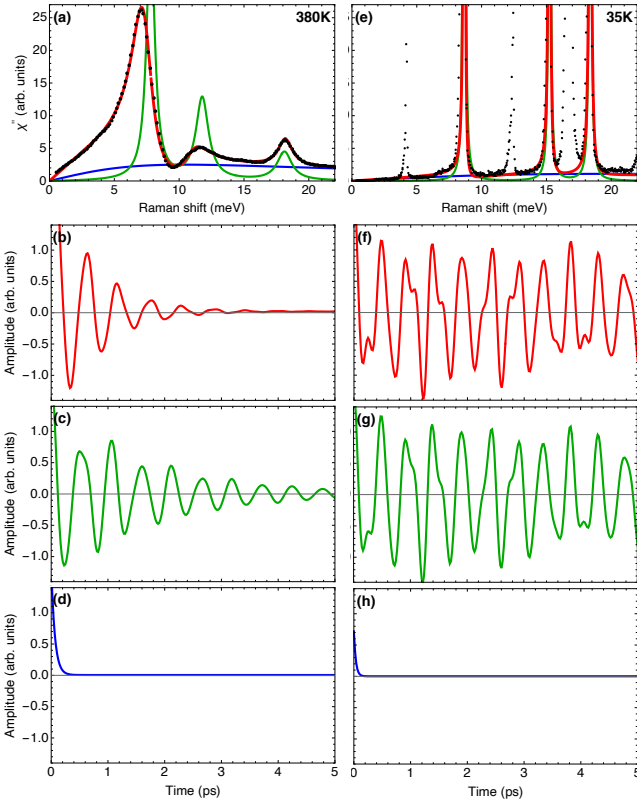


FIG. 22. Time-domain signal for the B_{2g} -symmetry excitations of Ta_2NiSe_5 . (a) The Raman response for Ta_2NiSe_5 measured in ac geometry at 380 K. The Fano fit [Eq. (B1)] is shown as the red curve; the bare phonon modes [Eq. (1)] are shown by the green curve; the bare excitonic continuum [Eq. (2)] is shown by the blue curve. The time-domain signal corresponding to the Fano fit, bare phonon modes, and bare excitonic continuum, obtained by inverse Fourier transform, are shown in (b), (c), and (d), respectively. (e) The Raman response for Ta_2NiSe_5 measured in ac geometry at 35 K. The corresponding time-domain signals are shown in (f), (g), and (h), respectively.

transition temperature, the phonon-exciton interaction significantly broadens the spectral features [Fig. 22(a)]; as a result the deduced time-resolved response decays fast and essentially dies out before 5 ps [Fig. 22(b)]. For the bare phononic response, the time-domain signal beyond 4 ps is dominated by the oscillation of 2 THz mode [Fig. 22(c)], corresponding to the $B_{2g}^{(1)}$ phonon. The signal of the bare excitonic response shows a pure relaxational behavior [Fig. 22(d)]. Comparing Fig. 22(b) and (c), we note that it is difficult to identify the Fano interference feature from time-domain signal, because such interference exhibits no distinct characters in the time domain, except for that the oscillations are strongly damped. Indeed, in ultrafast studies, the interference nature is not revealed even after Fourier transform of the time-domain data to the frequency domain [16, 17, 20]. The likely reason for that is the high pump fluence used, causing the exciton and phonon responses decouple already on the

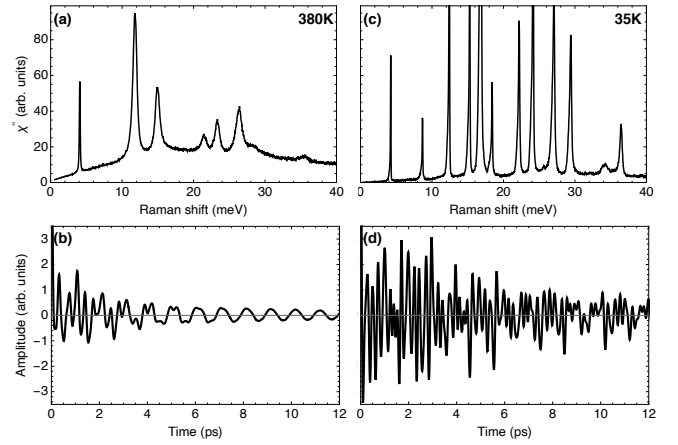


FIG. 23. Time-domain signal for the A_g -symmetry excitations of Ta_2NiSe_5 . (a) The Raman response for Ta_2NiSe_5 measured in aa geometry at 380 K. The time-domain signal, obtained by inverse Fourier transform of the data, is shown in (b). (c) The Raman response for Ta_2NiSe_5 measured in aa geometry at 35 K. The corresponding time-domain signal is shown in (d).

very early time scales.

Below the transition temperature, the energy at which the continuum has maximum response moves to higher energy, and the phonon-exciton coupling strength is reduced. Consequently, the interference effect is suppressed and the combined response is essentially the same as the bare phononic response [Fig. 22(f-g)]. The bare excitonic response still has a pure relaxational time dependence, with very short lifetime [Fig. 22(d) and (h)].

For comparison, in Fig. 23 we present the time-domain signal for the A_g -symmetry excitations. Above the transition temperature, although multiple oscillations are simultaneously present at short time scale, beyond 10 ps the time-domain signal is dominated by the oscillation of 1 THz [Fig. 23(b)], corresponding to the $A_g^{(1)}$ phonon mode whose spectral width is much smaller than others [Fig. 23(a)]. At low temperature, the difference between the spectral widths of various modes is reduced [Fig. 23(c)]; hence, these modes have comparable lifetime and multiple oscillations survive beyond 10 ps [Fig. 23(d)].

In relation to the ultra-fast studies of Ta_2NiSe_5 [15, 17, 58, 59], the Raman results are consistent with the ultra-fast data under low fluence. One ultra-fast work [17] provides evidence for coupling between the $A_g^{(1)}$ mode and the amplitude mode of the condensate under high-fluence pumping. We note that in our studies we can unambiguously identify the amplitude mode with the excitonic continuum we observe. Above the transition temperature, the overdamped excitonic mode softens on cooling towards T_c ; just below the transition temperature, its energy increases on further cooling. Such temperature dependence of mode energy is characteristic of an amplitude mode while the optical B_{2g} phonons only harden on

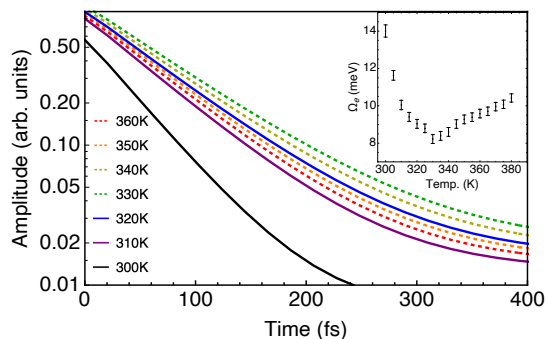


FIG. 24. Time-domain signal for the excitonic continuum of Ta_2NiSe_5 above and below the transition temperature, plotted in semi-log scale. The data above T_c are dashed for clarity. The relaxation time starts to decrease just below T_c . Inset: temperature dependence of the energy at which the excitonic continuum has maximum intensity, $\Omega_e(T)$.

cooling. In Fig. 24 we present the time-domain signal corresponding to the excitonic mode around the transition temperature.

Additionally, a mode associated with the phase of the excitonic order parameter may exist. The electron-phonon coupling and exchange interactions modify the otherwise sombrero-shape free-energy landscape, reducing the continuous $U(1)$ symmetry to a discrete Z_2 symmetry, leading to a finite energy of the phase mode. A recent pump-probe microscopy study suggests that the phase-mode energy is smaller than the $A_g^{(1)}$ -mode energy (around 4 meV) [58]. However, we do not observe any mode down to 0.4 meV at low temperature [Fig. 22(e)]. Furthermore, the phase oscillations of the order parameter should harden above T_c , which would have manifested itself in the low-energy range of the spectra. Such signatures are not observed, either [Fig. 6]. Therefore, existence of the phase mode below 4 meV is not supported by the Raman data.

VIII. CONCLUSIONS

We have employed polarization resolved Raman spectroscopy to conduct a systematic spectroscopic study of the lattice dynamics in $\text{Ta}_2\text{Ni}(\text{Se}_{1-x}\text{S}_x)_5$ ($x = 0, \dots, 1$) family of the excitonic insulators.

We identify and classify by symmetry all the Raman active phonon modes of A_g and B_{2g} symmetries. A change in selection rules is detected at temperature $T_c(x)$, indicating the orthorhombic-to-monoclinic structural phase transition related to the excitonic insulator state [23, 24]. We find that the symmetry breaking transition persists for entire $\text{Ta}_2\text{Ni}(\text{Se}_{1-x}\text{S}_x)_5$ family with $T_c(x)$ monotonically decreasing from 328 K for $x = 0$ to 120 K for $x = 1$. Its signatures in the resistivity data, however, become weak or undetectable for large sulfur concentration x that we attribute to the weakness of the

symmetry breaking at large x , demonstrated by the decrease of phonon intensity in the 'forbidden' scattering geometry.

For $x < 0.7$, the two lowest-frequency ac -quadrupole-symmetry $B_{2g}^{(1)}$ and $B_{2g}^{(2)}$ phonon modes show strongly asymmetric lineshapes at high temperatures, which is indicative of coupling between the phonons and an excitonic continuum of the same symmetry [23, 24]. Within the framework of extended Fano model, we develop a quantitative description of the observed lineshapes, enabling us to disentangle the excitonic and phononic contributions to the spectra, to derive the intrinsic phonon parameters and determine the exciton-phonon interaction strength, that affects the transition temperature $T_c(x)$ [24]. The displacement patterns obtained from *ab-initio* calculations explain the trends in the deduced exciton-phonon coupling values. At $T < T_c$ the remnant excitonic continuum demonstrates signatures of coupling to the finite-momentum B_{2g} -symmetry acoustic phonons, allowed due to scattering on a quasi-periodic structural of domain walls. We have also shown that the coupling to the excitonic continuum explains the acoustic mode softening observed in [24, 52].

The intrinsic parameters of the optical phonons for Ta_2NiSe_5 and Ta_2NiS_5 at low temperatures are mostly in good agreement with anharmonic decay model and DFT calculations. For alloy compositions a two-mode behavior is found for most modes, where signatures appear at two frequencies, corresponding to the ones in Ta_2NiSe_5 and Ta_2NiS_5 . However, several types of anomalous behavior have been observed in the temperature dependencies. For $x < 0.7$, the $B_{2g}^{(1)}$ and $B_{2g}^{(2)}$ modes anomalously harden close to T_c (e.g., Fig. 14), indicating an interaction with continuum beyond Fano model description [23]. For Ta_2NiS_5 (Fig. 18) the $B_{2g}^{(1)}$ and $B_{2g}^{(2)}$ modes do not show Fano shapes, but the frequencies of these modes anomalously soften on cooling, although never going critical. Finally, the intensity of the most modes is strongly temperature dependent. Interestingly, for Ta_2NiSe_5 we observe that the sum of electronic and phononic contributions to the aa static susceptibility is conserved (Fig. 19), pointing to an unexpected electron-phonon coupling mechanism within the excitonic insulator state.

In addition, based on our results we have provided an interpretation of recent time-resolved pump-probe experiments and discussed the signatures expected from the modes we have observed, see Figs. 22, 23 and 24. Overall, this work provides a comprehensive study lattice dynamics in $\text{Ta}_2\text{Ni}(\text{Se}_{1-x}\text{S}_x)_5$; more generally, the unconventional behaviors we observed point to the importance of the effects of electron-phonon coupling in correlated semimetals.

ACKNOWLEDGMENTS

M.Y. and P.A.V. contributed equally to this work. We acknowledge discussions with K. Haule. We are grateful to Y. Kauffmann for help with TEM measurements. The spectroscopic work conducted at Rutgers was supported by NSF Grant No. DMR-1709161 (M.Y. and G.B). P.A.V. acknowledges the Postdoctoral Fellowship support from the Rutgers University Center for Materials Theory. The sample growth and characterization work conducted at the Technion was supported by the Israel Science Foundation Grant No. 320/17 (H.L., I.F. and A.K.). H.L. was supported in part by a PBC fellowship of the Israel Council for Higher Education. The work at NICPB was supported by the Estonian Research Council Grant No. PRG736 and by the European Research Council (ERC) under Grant Agreement No. 885413. M.K. was supported by NSF DMREF grant DMR-1629059.

Appendix A: Estimation of heating in excitation laser spot

We use three methods to estimate the heating rate, a measure of the temperature increase per unit laser power in the focused laser spot (K/mW): (i) Stokes/anti-Stokes Raman scattering intensity ratio analysis; (ii) monitoring laser power that is inducing the phase transition; and (iii) a thermoconductivity model calculation. We use data for Ta_2NiSe_5 as an example to illustrate these methods.

For the first method, we note that the Stokes scattering cross section I_S and Anti-Stokes cross section I_{AS} are related by the detailed balance principle [22]

$$nI_S(\omega) = (n+1)I_{AS}(\omega), \quad (\text{A1})$$

in which n stands for the Bose factor

$$n(\omega, T) = \frac{1}{\exp(\hbar\omega/k_B T) - 1}, \quad (\text{A2})$$

where \hbar is the reduced Planck's constant, ω is frequency, k_B is the Boltzmann's constant, and T is the temperature in the laser spot.

Using Eq. (A1-A2), the temperature can be derived as

$$T = \frac{\hbar\omega}{k_B \ln(I_S/I_{AS})}, \quad (\text{A3})$$

or, numerically,

$$T[\text{K}] = \frac{11.605 \omega}{\ln(I_S/I_{AS})} [\text{meV}]. \quad (\text{A4})$$

We studied the Stokes and Anti-Stokes cross section relation for the ac scattering geometry at 295 K environmental temperature with various laser power. In Fig. 25 we show the results measured with 8 mW laser power as an example. The Raman responses calculated from Stokes and Anti-Stokes cross sections match well with

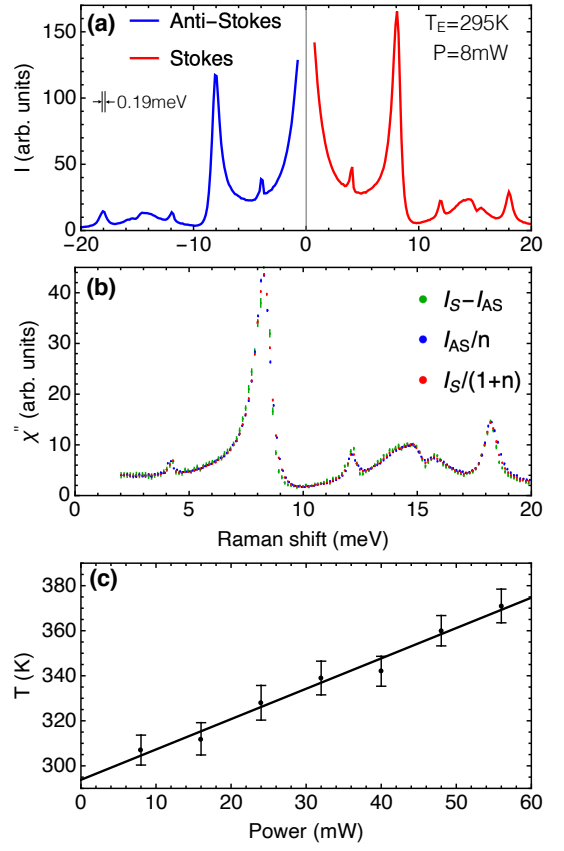


FIG. 25. Stokes-Anti-Stokes analysis of the ac spectra for Ta_2NiSe_5 . (a) The Stokes and Anti-Stokes cross sections measured at environmental temperature $T_E = 295\text{K}$ with laser power $P = 8\text{mW}$. (b) The Raman response calculated from the measured spectra in (a). The laser-spot temperature, which appears in the Bose factor n , is 307 K. The spectral resolution is 0.19 meV for panels (a-b). (c) The laser-power dependence of the laser-spot temperature. The straight line represents a linear fit.

the temperature at the laser spot being 307 K. We use Eq. (A4) with the phonon intensity integrated from 7.5 to 8.5 meV to calculate the temperature at the laser spot. By a linear fit to the power dependence of the laser-spot temperature, we find the heating rate to be $1.29 \pm 0.17\text{K/mW}$.

For the second method, we gradually increase laser power at 295 K environmental temperature. We find that when the laser power is in the range of $26 \pm 4\text{mW}$, the domain stripes, which are visible across the sample surface under laser illumination, disappear inside the laser spot. Moreover, the temperature dependence of phonon width and intensity has a sudden change. We assume that at this laser power, the temperature at the laser spot reaches the transition temperature 328 K [8, 9], yielding the heating rate of $1.25 \pm 0.20\text{K/mW}$. We note that for Ta_2NiS_5 , we do not observe domain stripes below its transition temperature 120 K. Its transition temperature is identified by the sudden change of phonon intensity,

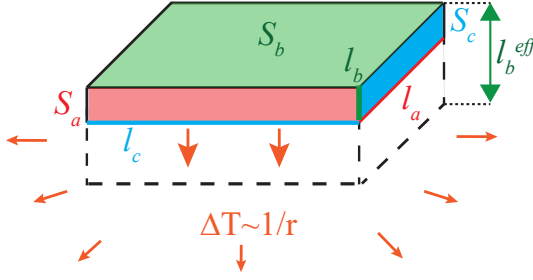


FIG. 26. The geometry of the heated volume. The lengths l_a and l_c are determined by the spot size, while l_b is approximated by the skin depth; the S_b is in the cleave plane facing the vacuum, while the other faces are in the bulk. Within the region marked by dashed lines, the heat flow is mostly along b axis, while outside the region heat flows in all directions comparably, such that the temperature increase above the base temperature ΔT decays as $1/r$, r being the distance from the heated region.

see Fig. 18(b) for example.

For the third method, we consider a heated region shown in Fig. 26 of a rectangular shape, with the dimensions given by the beam spot size and the penetration depth. The static heat equation takes the form:

$$-\kappa_x \frac{\partial^2 T}{\partial x^2} - \kappa_y \frac{\partial^2 T}{\partial y^2} - \kappa_z \frac{\partial^2 T}{\partial z^2} = \mathcal{P}(\mathbf{r}),$$

$$\left. \frac{\partial T(\mathbf{r})}{\partial z} \right|_{y=0} = 0; \quad (\text{A5})$$

$$\partial T(x \rightarrow \pm\infty, y \rightarrow -\infty, z \rightarrow \pm\infty) = T_0.$$

where $\mathcal{P}(\mathbf{r})$ is the power density. We ignore the cooling provided by the helium gas flow above the sample surface, so that there is no heat flow at the $y = 0$ boundary, while deep inside the bulk the temperature should reach the base temperature T_0 . Equation (A5) can be solved using Green's function of the Laplace equation and image method to satisfy the first boundary condition. In the latter, we extend the equation formally to $y > 0$ half-space and add an "image" power density

$$\mathcal{P}(x, y, z)\theta(-y) \rightarrow \mathcal{P}(x, y, z)\theta(-y) + \mathcal{P}(x, -y, z)\theta(y). \quad (\text{A6})$$

The solution is then given by:

$$T(\mathbf{r}) - T_0 = \int \frac{d\tilde{x}' d\tilde{y}' d\tilde{z}'}{4\pi} \frac{\mathcal{P}(\sqrt{\kappa_x}\tilde{x}', \dots)\theta(-\tilde{y}') + \tilde{y}' \rightarrow -\tilde{y}'}{|\tilde{\mathbf{r}} - \tilde{\mathbf{r}}'|}, \quad (\text{A7})$$

where $\tilde{\mathbf{r}} = (x/\sqrt{\kappa_x}, y/\sqrt{\kappa_y}, z/\sqrt{\kappa_z})$. The solution decays as $1/r$ at large distances and thus satisfies the second boundary condition of Eq. (A5). An analytical result can be obtained for

$$\mathcal{P}(x, y, z) = \frac{tP}{l_a l_b l_c} \theta(l_a/2 - |x|) \theta(l_b - |y|) \theta(l_c/2 - |z|) \quad (\text{A8})$$

at $\mathbf{r} = 0$ in the limit $l_b^2/\kappa_b \ll l_{a,c}^2/\kappa_{a,c}$, where P is the laser power and t is the transmission coefficient of the

sample. Performing the integral one obtains

$$T(0) - T_0 \approx \frac{tP \left(\frac{l_a}{\sqrt{\kappa_a}} \ln \frac{\frac{l_c}{\sqrt{\kappa_c}} + \sqrt{\frac{l_c^2}{\kappa_c} + \frac{l_a^2}{\kappa_a}}}{l_a/\sqrt{\kappa_a}} + a \leftrightarrow c \right)}{\sqrt{\kappa_b} \pi l_a l_c}. \quad (\text{A9})$$

Qualitatively, the result can be understood as follows. Due to the anisotropic shape of the heated region, right below it most heat is transferred along the b axis. However, the one-dimensional heat equation would result in a linear solution $T(y)$, depending on the cutoff scale l_c^{eff} . It can be estimated from the condition of the heat flow to the lateral direction being equal to the heat flow along b . Approximating the temperature gradient along a, b, c as $\Delta T/l_{a,b,c}$ one gets the condition

$$2l_b^{eff} l_a \kappa_c \frac{\Delta T}{l_c} + 2l_b^{eff} l_c \kappa_a \frac{\Delta T}{l_a} = l_a l_c \kappa_b \frac{\Delta T}{l_b^{eff}}, \quad (\text{A10})$$

that results in the estimate

$$l_b^{eff} = \sqrt{\frac{l_a^2 l_c^2 \kappa_b}{2l_a^2 \kappa_c + 2l_c^2 \kappa_a}}. \quad (\text{A11})$$

Equating the total heat flow outside this region to the input power one obtains the estimate

$$\Delta T \approx \frac{tP}{\sqrt{8\kappa_b(l_a^2 \kappa_c + l_c^2 \kappa_a)}}. \quad (\text{A12})$$

Overall, one notices that the temperature increase scales with the linear size of the spot. The laser heating power R is then determined as $\Delta T/P$; for the actual estimate we thus need to find the transmission coefficient t first.

The transmission coefficient can be calculated from the complex index of refraction n by the relationship $t = 1 - |(n-1)/(n+1)|^2$:

$$t = \frac{4n_1}{(n_1 + 1)^2 + n_2^2}, \quad (\text{A13})$$

in which n_1 and n_2 are the real and imaginary part of n . The complex index of refraction can be obtained from the complex dielectric constant ϵ by the relationship $\epsilon = n^2$:

$$n_1 = \sqrt{\frac{\sqrt{\epsilon_1^2 + \epsilon_2^2} + \epsilon_1}{2}}, n_2 = \sqrt{\frac{\sqrt{\epsilon_1^2 + \epsilon_2^2} - \epsilon_1}{2}}, \quad (\text{A14})$$

where ϵ_1 and ϵ_2 are the real and imaginary part of ϵ . The imaginary part ϵ_2 can be calculated from the real part of the optical conductivity σ_1 :

$$\epsilon_2 = \frac{60}{\omega} \sigma_1, \quad (\text{A15})$$

in which the unit of ω is cm^{-1} and that of σ_1 is $\Omega^{-1} \text{cm}^{-1}$. The polarization of the incoming light is along a -axis of the sample. Because the quantities ϵ_1 and σ_1 are 8.13 and

TABLE V. The various parameters used in calculating the laser heating rate at 295 K. The transmission coefficient is 0.64.

Quantity (unit)	a-axis	c-axis
κ (mWK ⁻¹ cm ⁻¹)	208	57.4
l (10 ⁻³ cm)	5	10

2.47Ω⁻¹cm⁻¹ respectively at the laser wavelength [55], we find t=0.64.

The experimentally measured thermal conductivity [60] at 295 K is $\kappa_a = 208$ mWK⁻¹cm⁻¹ and $\kappa_c = 57.4$ mWK⁻¹cm⁻¹.

The length scales $l_a = 5 \times 10^{-3}$ cm and $l_c = 1 \times 10^{-2}$ cm is determined by the $50 \times 100 \mu\text{m}^2$ laser spot. The length l_b is the skin depth, which is calculated from the imaginary part of the index of refraction n_2 :

$$l_b = \frac{1}{2\pi\omega n_2}, \quad (\text{A16})$$

in which the unit of ω is cm⁻¹ and that of l_b is cm. At the laser wavelength, $n_2=1.5$, and we find $l_b = 7 \times 10^{-6}$ cm (70 nm).

The known values for the variables in Eq. (A9) are summarized in Table V. Because κ_b is unknown, we cannot use Eq. (A9) to calculate the laser heating rate. However, if the heating rate is 1.29 K/mW at 295 K, as determined from the Stokes/anti-Stokes analysis, the value for κ_b should be 1.38 mWK⁻¹cm⁻¹.

An estimate for the electronic contribution to thermal conductivity $\kappa^{(e)}$ could be calculated from the electric resistivity ρ by virtue of Wiedemann-Franz law:

$$\kappa^{(e)} = \frac{LT}{\rho}, \quad (\text{A17})$$

in which $L = 2.44 \times 10^{-5}$ mWΩK⁻² is the Lorenz number. The resistivity along b axis at 295 K is $\rho_b = 2.34 \times 10^{-1}$ Ωcm [61], and we find $\kappa_b^{(e)} = 0.0308$ mWK⁻¹cm⁻¹. The ratio of $\kappa_b^{(e)}$ to κ_b is consistent with the ratios obtained along a and c axes [60]. Moreover, that $\kappa_b \ll \kappa_{a,c}$ is consistent with the quasi-2D structure of the system [62].

To illustrate that the laser heating rate is strongly temperature dependent, we use Eq. (A9) to calculate the heating rate as a function of temperature. The temperature dependence of κ_a and κ_c are taken from Ref. [60]. We assume that the ratio of κ_b to κ_c is temperature independent, and fix this ratio to be 1.38/57.4 = 2.40%. In Fig. 27 we show the calculated heating rate. Because of such assumption, the laser heating rate at 295 K is the same as that determined from the Stokes/anti-Stokes analysis.

Appendix B: The fitting model for the Fano interference

Above T_c , the $B_{2g}^{(1)}$ and $B_{2g}^{(2)}$ phonon modes of Ta₂NiSe₅ exhibit strongly asymmetric Fano lineshapes. To analyze the physics of this Fano interference features, we propose a model describing three phonon modes individually coupled to broad excitonic continuum. The total Raman response is described in the following way:

$$\chi'' \sim \Im T^T G T, \quad (\text{B1})$$

where $T^T = (T_{ph}^T \ t_e)$ denotes the vertices for light scattering process (the subscript "T" denotes "Transpose"), in which $T_{ph}^T = (t_{p1} \ t_{p2} \ t_{p3})$. G comprises the Green's functions for the interacting phononic and excitonic excitations that can be obtained by solving the Dyson equation:

$$G = (G_0^{-1} - V)^{-1}. \quad (\text{B2})$$

In Eq. (B2)

$$G_0 = \begin{pmatrix} G_{ph}^0 & 0 \\ 0 & G_e^0 \end{pmatrix} \quad (\text{B3})$$

is the bare Green's function and

$$V = \begin{pmatrix} 0 & V_{e-ph} \\ V_{e-ph}^T & 0 \end{pmatrix} \quad (\text{B4})$$

is the exciton-phonon interaction. Here the bare phononic Green's function

$$G_{ph}^0 = \text{diag}[G_{pi}^0] \\ = \text{diag}\left[-\left(\frac{1}{\omega - \omega_{pi} + i\gamma_{pi}} - \frac{1}{\omega + \omega_{pi} + i\gamma_{pi}}\right)\right], \quad (\text{B5})$$

correspond to the $B_{2g}^{(i)}$ -symmetry phonon modes (i=1,2,3),

$$G_e = \frac{1}{\omega_e^2/\gamma_e - i\omega} \quad (\text{B6})$$

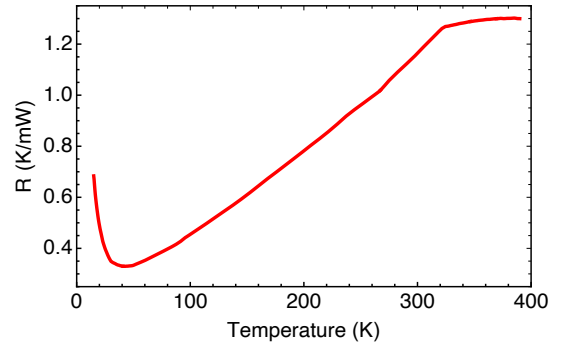


FIG. 27. Temperature dependence of the laser heating rate R , calculated by Eq. (A9) with the thermal conductivity data taken from Ref. [60].

represents the excitonic continuum, and $V_{e-ph}^T = (v_1 \ v_2 \ v_3)$ denotes exciton interaction strength with the corresponding phonons. For phononic equation, the parameters ω_{pi} and γ_{pi} have the meaning of the mode frequency and the half width at half maximum (HWHM), respectively. For the excitonic equation, ω_e is the energy of the overdamped excitations and γ_e represents the relaxation rate. The quantity $\Omega_e = \omega_e^2/\gamma_e$ denotes the energy at which the excitonic continuum has maximum intensity.

The bare phononic and excitonic responses are

$$\chi_p''^{(0)} = \Im T_{ph}^T G_{ph}^0 T_{ph} = \sum_{i=1}^3 t_{pi}^2 \Im G_{pi}^0 \quad (\text{B7})$$

and

$$\chi_e''^{(0)} = t_e^2 \Im G_e^0. \quad (\text{B8})$$

These two expressions are related to Eqsw. (1-2) in the main text.

The renormalized phononic and excitonic responses, χ_p'' and χ_e'' , as well as the interference term χ_{int}'' are calculated from the renormalized Green's function G :

$$G = \begin{pmatrix} G_{ph} & G_{e-ph} \\ G_{e-ph}^T & G_e \end{pmatrix}, \quad (\text{B9})$$

where $G_{e-ph}^T = (G_{1e} \ G_{2e} \ G_{3e})$ represents the interference between the phononic modes and the continuum.

The phononic term is calculated from the 3x3 phononic block:

$$\chi_p'' = \Im T_{ph}^T G_{ph} T_{ph}; \quad (\text{B10})$$

the excitonic term results from the 1x1 excitonic block:

$$\chi_e'' = t_e^2 \Im G_e; \quad (\text{B11})$$

and the interference term is given by the off-diagonal block

$$\chi_{int}'' = t_e \sum_{i=1}^3 t_{pi} \Im G_{ie}. \quad (\text{B12})$$

These three terms, as defined, satisfy Eq. (4):

$$\chi'' = \chi_p'' + \chi_e'' + \chi_{int}''. \quad (\text{B13})$$

For the *ac* spectra below T_c , especially at about 300 K, this model cannot properly account for the low frequency Raman response. This additional spectral feature is related to Raman coupling to the longitudinal acoustic excitations at finite momenta in the presence of quasi-periodic domain walls, detailed in the main text. The Green's function of each individual acoustic mode has form similar to the phononic Green's function:

$$G_s(\omega, q) = -\left(\frac{1}{\omega - c_s q + i r_s q} - \frac{1}{\omega + c_s q + i r_s q} \right). \quad (\text{B14})$$

Its light-scattering vertex $t_s(q)$ and coupling to the excitonic continuum $v_s(q)$ are both proportional to the square root of wavevector: $t_s = \tau_s \sqrt{q}$ and $v_s = \beta_s \sqrt{q}$. The frequency ω_s and the HWHM γ_s are both proportional to the wavevector: $\omega_s = c_s q$ and $\gamma_s = r_s q$.

After introducing this mode, Eqs. (B3-B4) extend to

$$G'_0 = \begin{pmatrix} G_{ph}^0 & 0 & 0 \\ 0 & G_s & 0 \\ 0 & 0 & G_e \end{pmatrix}, \quad (\text{B15})$$

$$V' = \begin{pmatrix} 0 & 0 & V_{e-ph} \\ 0 & 0 & \beta_s \sqrt{q} \\ V_{e-ph}^T & \beta_s \sqrt{q} & 0 \end{pmatrix}, \quad (\text{B16})$$

and the vertex for light-scattering process becomes $T'^T = \begin{pmatrix} T_{ph}^T & \tau_s \sqrt{q} & t_e \end{pmatrix}$.

Then the total response function containing coupling to acoustic mode for domain walls i lattice constants apart is given by

$$\chi_i'' \sim \Im T'^T G' T'. \quad (\text{B17})$$

Due to the requirement of causality, the real part of susceptibility should be an even function while the imaginary part should be an odd function. Therefore, the static Raman susceptibility is purely real. The total static Raman susceptibility is given by

$$\chi(\omega = 0) \sim \Re T^T G(\omega = 0) T. \quad (\text{B18})$$

The bare phononic static Raman susceptibility can be obtained from

$$\chi_p^{(0)}(\omega = 0) \sim \Re T_{ph}^T G_{ph}^0(\omega = 0) T_{ph} = \sum_{i=1}^3 \frac{2t_{pi}^2 \omega_{pi}}{\omega_{pi}^2 + \gamma_{pi}^2}, \quad (\text{B19})$$

Similarly, the bare excitonic static Raman susceptibility is given by

$$\chi_e^{(0)}(\omega = 0) \sim t_e^2 \Re G_e^0(\omega = 0) = \frac{t_e^2}{\Omega_e}, \quad (\text{B20})$$

For temperature-independent t_e , the temperature dependence of $1/\chi_e$ directly follows that of $\Omega_e(T) = \omega_e^2/\gamma_e$.

Using the Green's function G' , which describes the interacting phononic (both optical and acoustic) and excitonic excitations, we can evaluate the renormalization of sound velocity above T_c . Because the relevant frequencies for the acoustic mode are much lower than that of the optical or excitonic modes, we can keep ω only in the bare acoustic mode's Green's function:

$$G^* = \begin{pmatrix} \frac{\omega_{p1}}{2} & 0 & 0 & 0 & -v_1 \\ 0 & \frac{\omega_{p2}}{2} & 0 & 0 & -v_2 \\ 0 & 0 & \frac{\omega_{p3}}{2} & 0 & -v_3 \\ 0 & 0 & 0 & -\frac{\omega^2 - c_s^2 q^2}{2c_s q} & -\beta_s \sqrt{q} \\ -v_1 & -v_2 & -v_3 & -\beta_s \sqrt{q} & \Omega_e \end{pmatrix}^{-1}, \quad (\text{B21})$$

in which finite linewidths of phonon modes are neglected. The pole of this Green's function is obtained by requiring the determinant of inverse G^* to be zero:

$$\frac{\omega^2 - c_s^2 q^2}{2c_s q} = -\frac{\beta_s^2 q}{\Omega_e - \sum_{i=1}^3 \frac{2v_i^2}{\omega_{pi}}}. \quad (\text{B22})$$

Identifying ω^2 as $\tilde{c}_s^2 q^2$, in which \tilde{c}_s represents the renormalized sound velocity above T_c , we have

$$\tilde{c}_s^2 = c_s^2 - \frac{2\beta_s^2 c_s}{\Omega_e - \sum_{i=1}^3 \frac{2v_i^2}{\omega_{pi}}}. \quad (\text{B23})$$

Appendix C: Illustration of the fitting model for the Fano interference

To provide more insights into the fitting model described in Appendix B, we consider a simplified case in which only one phonon mode couples to an excitonic continuum. When exciton-phonon interaction v is zero, the total Raman response is reduced to the sum of the excitonic component and the phononic component:

$$\chi_0''(\omega) = \frac{t_e^2 \omega}{\Omega_e^2 + \omega^2} + \frac{4t_p^2 \gamma_p \omega_p \omega}{(\omega^2 - \omega_p^2)^2 + 2\gamma_p^2(\omega^2 + \omega_p^2) + \gamma_p^4}, \quad (\text{C1})$$

in which Ω_e stands for ω_e^2/γ_e .

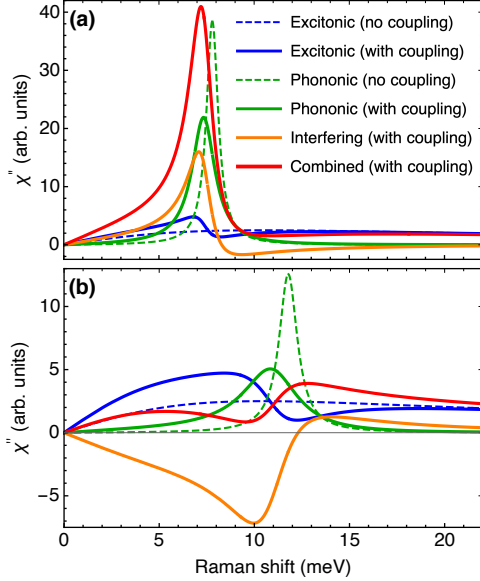


FIG. 28. Coupling of the excitonic continuum with (a) the $B_{2g}^{(1)}$ phonon mode and (b) the $B_{2g}^{(2)}$ phonon mode. The parameters used for plotting are obtained from fitting the 380 K spectrum of Ta_2NiSe_5 . The Raman response $\chi''(\omega)$ of the excitonic and phononic excitations for cases without (dashed lines) and with (solid lines) the effect of coupling are compared. The solid red lines correspond to the addition of the solid blue, solid green, and solid orange lines.

In Fig. 28 we show the excitonic continuum coupling with the $B_{2g}^{(1)}$ and $B_{2g}^{(2)}$ phonon modes in an individually way to illustrate the effect of coupling. First we discuss the renormalization effect. The renormalized phonon mode shifts in energy and broadens in lineshape. If we neglect the bare phonon width γ_p for simplicity, the central energy of the renormalized phonon mode, ω_{pv} , can be expressed as

$$\omega_{pv} = \omega_p + \frac{v^2(v^2 - 2\omega_p\Omega_e)}{2(v^2\Omega_e + \omega_p\Omega_e^2 + \omega_p^3)}. \quad (\text{C2})$$

For both the $B_{2g}^{(1)}$ and $B_{2g}^{(2)}$ phonon modes, v^2 is smaller than $2\omega_p\Omega_e$; therefore ω_{pv} is smaller than ω_p , meaning the renormalized phonon mode shifts to lower energy. Interestingly, at frequency ω_{pv} the renormalized excitonic continuum has the same intensity as the unrenormalized continuum; below ω_{pv} the excitonic response is enhanced while above ω_{pv} the excitonic response is suppressed.

Second we discuss the interference effect. For the interference term, corresponding to the off-diagonal elements of the renormalized Green's function, there is a frequency ω_{int} at which it changes the sign. The frequency ω_{int} has the following expression

$$\omega_{int} = \sqrt{2\Omega_e\gamma_p + \gamma_p^2 + \omega_p^2}. \quad (\text{C3})$$

We note that ω_{int} is a bit larger than ω_p . The shape of the interference term is controlled by sign of v : for positive v , below the zero-intensity point the interference term has

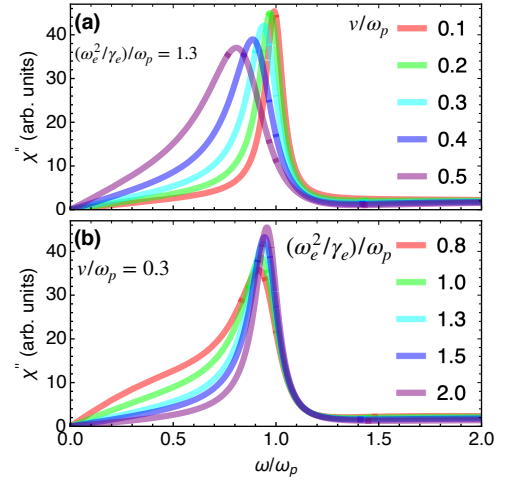


FIG. 29. The influence of the coupling strength v , and the frequency at which the excitonic continuum has maximum intensity $\Omega_e = \omega_e^2/\gamma_e$ on the Raman response $\chi''(\omega)$ of the coupled excitonic and phononic modes. (a) The combined response for varying v/ω_p with fixed $\Omega_e/\omega_p=1.3$; (b) The combined response for varying Ω_e/ω_p with fixed $v/\omega_p=0.3$. For all panels, $t_p=3.8$ arb. units; $t_e=7.2$ arb. units; $\omega_p=7.8$ meV; $\gamma_p=0.38$ meV. The ratios derived from the 380 K spectrum of Ta_2NiSe_5 are $\Omega_e/\omega_p=1.3$ and $v/\omega_p=0.3$. The horizontal axis is normalized to the phonon frequency ω_p .

positive intensity while the intensity is negative above the zero-intensity point; for negative v , the opposite is true. Far away from the resonance, the interference term decays to zero because the phonon mode has negligible intensity at such high energy.

Finally we note that when ω is much larger than ω_p and γ_e , the Raman response is In Fig. 29 we show how the coupling strength v , and the energy at which the excitonic continuum has maximum intensity $\Omega_e = \omega_e^2/\gamma_e$ influence the combined Raman response. The lineshape becomes more asymmetric with increasing v/ω_p [Fig. 29 (a)]. When Ω_e is varied, we find that the lineshape becomes more asymmetric for smaller Ω_e [Fig. 29 (b)].

approximately t_e^2/ω . Therefore, t_e can be determined by fitting the data at large ω .

Appendix D: The fitted parameters of the anharmonic decay model for Ta_2NiSe_5 and Ta_2NiS_5

The temperature dependence of both frequency and FWHM for the most phonon modes of Ta_2NiSe_5 and Ta_2NiS_5 modes can be accounted by the anharmonic decay model [Eq. (16-17)]. The values for the parameters from fitting are summarized in Table VI.

TABLE VI. The fitting parameters of the anharmonic decay model [Eq. (16-17)] for the Raman-active optical phonon modes of $\text{Ta}_2\text{Ni}(\text{Se}_{1-x}\text{S}_x)_5$ family. The frequencies and FWHM below the phase transition temperature are fitted. The anharmonic decay model is not applicable for the B_{2g} -symmetry modes of Ta_2NiS_5 . The units are in meV.

Mode	ω_0	ω_2	Γ_0	Γ_2
Ta_2NiSe_5				
$A_g^{(1)}$	4.235(16)	0.0038(10)	0.06(4)	0.0014(15)
$B_{2g}^{(1)}$	8.721(5)	0.0290(11)	0.073(15)	0.019(3)
$A_g^{(2)}$	12.484(12)	0.0405(22)	0.09(3)	0.025(6)
$B_{2g}^{(2)}$	15.35(4)	0.070(15)	0.05(10)	0.09(4)
$A_g^{(3)}$	17.077(12)	0.191(5)	0.08(5)	0.114(23)
$B_{2g}^{(3)}$	18.45(3)	0.050(16)	0.11(10)	0.08(5)
$A_g^{(4)}$	22.28(3)	0.082(15)	0.12(8)	0.05(4)
$A_g^{(5)}$	24.287(11)	0.129(6)	0.05(3)	0.072(15)
$A_g^{(6)}$	27.17(4)	0.137(16)	0.23(11)	0.09(5)
$A_g^{(7)}$	29.62(6)	0.21(3)	0.18(16)	0.12(9)
$A_g^{(8)}$	36.75(14)	0.30(8)	0.3(4)	0.09(24)
$\text{Ta}_2\text{Ni}(\text{Se}_{0.75}\text{S}_{0.25})_5$				
$A_g^{(1)}$	4.277(16)	0.0039(9)	0.12(5)	0.0025(34)
$B_{2g}^{(1)}$	8.758(7)	0.0322(15)	0.252(21)	0.028(4)
$\text{Ta}_2\text{Ni}(\text{Se}_{0.33}\text{S}_{0.67})_5$				
$A_g^{(1)}$	4.630(12)	0.0048(8)	0.10(2)	0.0012(11)
$B_{2g}^{(1)}$	8.739(19)	0.032(4)	0.479(26)	0.022(4)
Ta_2NiS_5				
$A_g^{(1)}$	5.025(10)	0.0040(7)	0.068(25)	0.0014(19)
$A_g^{(2)}$	16.198(4)	0.0610(13)	0.051(9)	0.0359(26)
$A_g^{(3)}$	19.276(11)	0.134(4)	0.11(3)	0.070(11)
$A_g^{(4)}$	33.92(4)	0.111(19)	0.28(11)	0.15(6)
$A_g^{(5)}$	36.634(10)	0.138(5)	0.056(28)	0.112(16)
$A_g^{(6)}$	40.29(20)	0.21(12)	0.6(7)	0.3(4)
$A_g^{(7)}$	43.39(6)	0.29(4)	0.01(14)	0.17(9)
$A_g^{(8)}$	49.72(3)	0.23(3)	0.04(10)	0.45(8)

- [1] W. Kohn, Excitonic phases, *Physical Review Letters* **19**, 439 (1967).
- [2] B. I. Halperin and T. M. Rice, Possible anomalies at a semimetal-semiconductor transition, *Rev. Mod. Phys.* **40**, 755 (1968).
- [3] W. Kohn and D. Sherrington, Two kinds of bosons and Bose condensates, *Rev. Mod. Phys.* **42**, 1 (1970).
- [4] T. Pillo, J. Hayoz, H. Berger, F. Lévy, L. Schlapbach, and P. Aebi, Photoemission of bands above the Fermi level: The excitonic insulator phase transition in $1T - \text{TiSe}_2$, *Phys. Rev. B* **61**, 16213 (2000).
- [5] H. Cercellier, C. Monney, F. Clerc, C. Battaglia, L. Despont, M. G. Garnier, H. Beck, P. Aebi, L. Patthey, H. Berger, and L. Forró, Evidence for an Excitonic Insulator Phase in $1T - \text{TiSe}_2$, *Phys. Rev. Lett.* **99**, 146403 (2007).
- [6] C. Monney, C. Battaglia, H. Cercellier, P. Aebi, and H. Beck, Exciton Condensation Driving the Periodic Lattice Distortion of $1T - \text{TiSe}_2$, *Phys. Rev. Lett.* **106**, 106404 (2011).
- [7] A. Kogar, M. S. Rak, S. Vig, A. A. Husain, F. Flicker, Y. I. Joe, L. Venema, G. J. MacDougall, T. C. Chiang, E. Fradkin, J. van Wezel, and P. Abbamonte, Signatures of exciton condensation in a transition metal dichalcogenide, *Science* **358**, 1314 (2017).
- [8] Y. F. Lu, H. Kono, T. I. Larkin, A. W. Rost, T. Takayama, A. V. Boris, B. Keimer, and H. Takagi, Zero-gap semiconductor to excitonic insulator transition in Ta_2NiSe_5 , *Nat. Commun.* **8**, 14408 (2017).
- [9] F. D. Salvo, C. Chen, R. Fleming, J. Waszczak, R. Dunn, S. Sunshine, and J. A. Ibers, Physical and structural properties of the new layered compounds Ta_2NiS_5 and Ta_2NiSe_5 , *J. Less Common. Met.* **116**, 51 (1986).
- [10] Y. Wakisaka, T. Sudayama, K. Takubo, T. Mizokawa, M. Arita, H. Namatame, M. Taniguchi, N. Katayama, M. Nohara, and H. Takagi, Excitonic Insulator State in Ta_2NiSe_5 Probed by Photoemission Spectroscopy, *Phys. Rev. Lett.* **103**, 026402 (2009).
- [11] K. Seki, Y. Wakisaka, T. Kaneko, T. Toriyama, T. Konishi, T. Sudayama, N. L. Saini, M. Arita, H. Namatame, M. Taniguchi, N. Katayama, M. Nohara, H. Takagi, T. Mizokawa, and Y. Ohta, Excitonic Bose-Einstein condensation in Ta_2NiSe_5 above room temperature, *Phys. Rev. B* **90**, 155116 (2014).
- [12] M. D. Watson, I. Marković, E. A. Morales, P. Le Fèvre, M. Merz, A. A. Haghighirad, and P. D. C. King, Band hybridization at the semimetal-semiconductor transition of Ta_2NiSe_5 enabled by mirror-symmetry breaking, *Phys. Rev. Research* **2**, 013236 (2020).
- [13] S. Mor, M. Herzog, D. Golež, P. Werner, M. Eckstein, N. Katayama, M. Nohara, H. Takagi, T. Mizokawa, C. Monney, and J. Stähler, Ultrafast electronic band gap control in an excitonic insulator, *Phys. Rev. Lett.* **119**, 086401 (2017).
- [14] Y. Murakami, D. Golež, M. Eckstein, and P. Werner, Photoinduced enhancement of excitonic order, *Phys. Rev. Lett.* **119**, 247601 (2017).
- [15] Q. M. Liu, D. Wu, Z. A. Li, L. Y. Shi, Z. X. Wang, S. J. Zhang, T. Lin, T. C. Hu, H. F. Tian, J. Q. Li, T. Dong, and N. L. Wang, Photoinduced multistage phase transitions in Ta_2NiSe_5 , *Nature Communications* **12**, 2050 (2021).
- [16] H. Ning, O. Mehio, M. Buchhold, T. Kurumaji, G. Refael, J. G. Checkelsky, and D. Hsieh, Signatures of Ultrafast Reversal of Excitonic Order in Ta_2NiSe_5 , *Phys. Rev. Lett.* **125**, 267602 (2020).
- [17] D. Werdehausen, T. Takayama, M. Höppner, G. Albrecht, A. W. Rost, Y. Lu, D. Manske, H. Takagi, and S. Kaiser, Coherent order parameter oscillations in the ground state of the excitonic insulator Ta_2NiSe_5 , *Science Advances* **4**, aap8652 (2018).
- [18] T. Kaneko, T. Toriyama, T. Konishi, and Y. Ohta, Orthorhombic-to-monoclinic phase transition of Ta_2NiSe_5 induced by the Bose-Einstein condensation of excitons, *Phys. Rev. B* **87**, 035121 (2013).
- [19] G. Mazza, M. Rösner, L. Windgätter, S. Latini, H. Hübener, A. J. Millis, A. Rubio, and A. Georges, Nature of Symmetry Breaking at the Excitonic Insulator Transition: Ta_2NiSe_5 , *Phys. Rev. Lett.* **124**, 197601 (2020).
- [20] E. Baldini, A. Zong, D. Choi, C. Lee, M. H. Michael, L. Windgätter, I. I. Mazin, S. Latini, D. Azouy, B. Lv, A. Kogar, Y. Wang, Y. Lu, T. Takayama, H. Takagi, A. J. Millis, A. Rubio, E. Demler, and N. Gedik, The spontaneous symmetry breaking in Ta_2NiSe_5 is structural in nature (2020), [arXiv:2007.02909](https://arxiv.org/abs/2007.02909) [cond-mat.str-el].
- [21] Y. Chiba, T. Mitsuoka, N. L. Saini, K. Horiba, M. Kobayashi, K. Ono, H. Kumigashira, N. Katayama, H. Sawa, M. Nohara, Y. F. Lu, H. Takagi, and T. Mizokawa, Valence-bond insulator in proximity to excitonic instability, *Phys. Rev. B* **100**, 245129 (2019).
- [22] W. Hayes and R. Loudon, *Scattering of Light by Crystals* (John Wiley and Sons, New York, 1978).
- [23] P. A. Volkov, M. Ye, H. Lohani, I. Feldman, A. Kanigel, and G. Blumberg, Critical charge fluctuations and emergent coherence in a strongly correlated excitonic insulator, *npj Quant. Mater.* **6**, 52 (2021).
- [24] P. A. Volkov, M. Ye, H. Lohani, I. Feldman, A. Kanigel, and G. Blumberg, Failed excitonic quantum phase transition in $\text{Ta}_2\text{Ni}(\text{Se}_{1-x}\text{S}_x)_5$, An accompanying paper (2021), [arXiv:2104.07032](https://arxiv.org/abs/2104.07032) [cond-mat.str-el].
- [25] P. E. Blöchl, Projector augmented-wave method, *Phys. Rev. B* **50**, 17953 (1994).
- [26] J. P. Perdew, K. Burke, and M. Ernzerhof, Generalized gradient approximation made simple, *Phys. Rev. Lett.* **77**, 3865 (1996).
- [27] P. Giannozzi, O. Andreussi, T. Brumme, O. Bunau, M. B. Nardelli, M. Calandra, R. Car, C. Cavazzoni, D. Ceresoli, M. Cococcioni, N. Colonna, I. Carnimeo, A. D. Corso, S. de Gironcoli, P. Delugas, R. A. DiStasio, A. Ferretti, A. Floris, G. Fratesi, G. Fugallo, R. Gebauer, U. Gerstmann, F. Giustino, T. Gorni, J. Jia, M. Kawamura, H.-Y. Ko, A. Kokalj, E. Küçükbenli, M. Lazzeri, M. Marsili, N. Marzari, F. Mauri, N. L. Nguyen, H.-V. Nguyen, A. O. de-la Roza, L. Paulatto, S. Poncé, D. Rocca, R. Sabatini, B. Santra, M. Schlipf, A. P. Seitsonen, A. Smogunov, I. Timrov, T. Thonhauser, P. Umari, N. Vast, X. Wu, and S. Baroni, Advanced capabilities for materials modelling with quantum ESPRESSO, *Journal of Physics: Condensed Matter* **29**, 465901 (2017).

- [28] A. Dal Corso, Pseudopotentials periodic table: From H to Pu, *Computational Materials Science* **95**, 337 (2014).
- [29] S. Grimme, Semiempirical gga-type density functional constructed with a long-range dispersion correction, *J. Comput. Chem.* **27**, 1787 (2006).
- [30] G. Kresse and J. Furthmüller, Efficiency of ab-initio total energy calculations for metals and semiconductors using a plane-wave basis set, *Computational Materials Science* **6**, 15 (1996).
- [31] G. Kresse and J. Furthmüller, Efficient iterative schemes for ab initio total-energy calculations using a plane-wave basis set, *Phys. Rev. B* **54**, 11169 (1996).
- [32] A. Togo and I. Tanaka, First principles phonon calculations in materials science, *Scripta Materialia* **108**, 1 (2015).
- [33] A. Nakano, K. Sugawara, S. Tamura, N. Katayama, K. Matsubayashi, T. Okada, Y. Uwatoko, K. Munakata, A. Nakao, H. Sagayama, R. Kumai, K. Sugimoto, N. Maejima, A. Machida, T. Watanuki, and H. Sawa, Pressure-induced coherent sliding-layer transition in the excitonic insulator Ta_2NiSe_5 , *IUCrJ* **5**, 158 (2018).
- [34] S. A. Sunshine and J. A. Ibers, Structure and physical properties of the new layered ternary chalcogenides tantalum nickel sulfide (Ta_2NiS_5) and tantalum nickel selenide (Ta_2NiSe_5), *Inorganic Chemistry* **24**, 3611 (1985).
- [35] R. J. Elliott, J. A. Krumhansl, and P. L. Leath, The theory and properties of randomly disordered crystals and related physical systems, *Rev. Mod. Phys.* **46**, 465 (1974).
- [36] A. S. Barker and A. J. Sievers, Optical studies of the vibrational properties of disordered solids, *Rev. Mod. Phys.* **47**, S1 (1975).
- [37] L. Bergman and R. J. Nemanich, Raman Spectroscopy for Characterization of Hard, Wide-Bandgap Semiconductors: Diamond, GaN, GaAlN, AlN, BN, *Annu. Rev. Mater. Sci.* **26**, 551 (1996).
- [38] S. Y. Kim, Y. Kim, C.-J. Kang, E.-S. An, H. K. Kim, M. J. Eom, M. Lee, C. Park, T.-H. Kim, H. C. Choi, B. I. Min, and J. S. Kim, Layer-Confined Excitonic Insulating Phase in Ultrathin Ta_2NiSe_5 Crystals, *ACS Nano* **10**, 8888 (2016).
- [39] J. Yan, R. Xiao, X. Luo, H. Lv, R. Zhang, Y. Sun, P. Tong, W. Lu, W. Song, X. Zhu, and Y. Sun, Strong Electron-Phonon Coupling in the Excitonic Insulator Ta_2NiSe_5 , *Inorganic Chemistry* **58**, 9036 (2019), pMID: 31246443.
- [40] M.-J. Kim, A. Schulz, T. Takayama, M. Isobe, H. Takagi, and S. Kaiser, Phononic soft mode behavior and a strong electronic background across the structural phase transition in the excitonic insulator Ta_2NiSe_5 , *Phys. Rev. Research* **2**, 042039 (2020).
- [41] K. Kim, H. Kim, J. Kim, C. Kwon, J. S. Kim, and B. J. Kim, Direct observation of excitonic instability in Ta_2NiSe_5 , *Nature Communications* **12**, 1969 (2021).
- [42] K. Kim, H. Kim, J. Kim, C. Kwon, J. S. Kim, and B. J. Kim, Author Correction: Direct observation of excitonic instability in Ta_2NiSe_5 , *Nature Communications* **12**, 2998 (2021).
- [43] A. Subedi, Orthorhombic-to-monoclinic transition in Ta_2NiSe_5 due to a zone-center optical phonon instability, *Phys. Rev. Materials* **4**, 083601 (2020).
- [44] A. S. Barker and R. Loudon, Response functions in the theory of raman scattering by vibrational and polariton modes in dielectric crystals, *Rev. Mod. Phys.* **44**, 18 (1972).
- [45] U. Fano, Effects of configuration interaction on intensities and phase shifts, *Phys. Rev.* **124**, 1866 (1961).
- [46] M. V. Klein, Electronic Raman scattering, in *Light Scattering in Solids I*, Vol. 8, edited by M. Cardona (Springer-Verlag, Berlin, 1983) Chap. 4, pp. 147–202.
- [47] G. Blumberg, M. V. Klein, L. Börjesson, R. Liang, and W. N. Hardy, Investigation of the temperature dependence of electron and phonon Raman scattering in single crystal $\text{YBa}_2\text{Cu}_3\text{O}_{6.952}$, *J. Supercond.* **7**, 445 (1994).
- [48] Note that the interaction-induced linewidth γ_p^v is often significantly larger than the bare width γ_p , which is the case for presented data above T_c . Consequently, an analysis of the phonon lineshape that does not explicitly include the interaction with the continuum (e.g. by simply adding the intensities of Fano-shaped phonons and the continuum) would lead to an erroneous large intrinsic phonon linewidth.
- [49] Note that the cubic term in the denominator can be neglected as long as the frequency is not far from ω_p .
- [50] Y. Gallais and I. Paul, Charge nematicity and electronic raman scattering in iron-based superconductors, *Comptes Rendus Physique* **17**, 113 (2016).
- [51] A. E. Böhmer, P. Burger, F. Hardy, T. Wolf, P. Schweiss, R. Fromknecht, M. Reinecker, W. Schranz, and C. Meingast, Nematic Susceptibility of Hole-Doped and Electron-Doped BaFe_2As_2 Iron-Based Superconductors from Shear Modulus Measurements, *Phys. Rev. Lett.* **112**, 047001 (2014).
- [52] A. Nakano, T. Hasegawa, S. Tamura, N. Katayama, S. Tsutsui, and H. Sawa, Antiferroelectric distortion with anomalous phonon softening in the excitonic insulator Ta_2NiSe_5 , *Phys. Rev. B* **98**, 045139 (2018).
- [53] H.-H. Kung, M. Salehi, I. Boulares, A. F. Kemper, N. Koirala, M. Brahlek, P. Lošťák, C. Uher, R. Merlin, X. Wang, S.-W. Cheong, S. Oh, and G. Blumberg, Surface vibrational modes of the topological insulator Bi_2Se_3 observed by Raman spectroscopy, *Phys. Rev. B* **95**, 245406 (2017).
- [54] Chauvière, L. and Gallais, Y. and Cazayous, M. and Méasson, M. A. and Sacuto, A. and Colson, D. and Forget, A., Raman scattering study of spin-density-wave order and electron-phonon coupling in $\text{Ba}(\text{Fe}_{1-x}\text{Co}_x)_2\text{As}_2$, *Phys. Rev. B* **84**, 104508 (2011).
- [55] T. I. Larkin, A. N. Yaresko, D. Pröpper, K. A. Kikoin, Y. F. Lu, T. Takayama, Y.-L. Mathis, A. W. Rost, H. Takagi, B. Keimer, and A. V. Boris, Giant exciton Fano resonance in quasi-one-dimensional Ta_2NiSe_5 , *Phys. Rev. B* **95**, 195144 (2017).
- [56] P. G. Klemens, Anharmonic Decay of Optical Phonons, *Phys. Rev.* **148**, 845 (1966).
- [57] K. Mu, H. Chen, Y. Li, Y. Zhang, P. Wang, B. Zhang, Y. Liu, G. Zhang, L. Song, and Z. Sun, Electronic structures of layered Ta_2NiS_5 single crystals revealed by high-resolution angle-resolved photoemission spectroscopy, *J. Mater. Chem. C* **6**, 3976 (2018).
- [58] P. Andrich, H. M. Bretscher, Y. Murakami, D. Golež, B. Remez, P. Telang, A. Singh, L. Harnagea, N. R. Cooper, A. J. Millis, P. Werner, A. K. Sood, and A. Rao, Imaging the coherent propagation of collective modes in the excitonic insulator candidate Ta_2NiSe_5 at room temperature (2020), [arXiv:2003.10799 \[cond-mat.str-el\]](https://arxiv.org/abs/2003.10799).
- [59] H. M. Bretscher, P. Andrich, P. Telang, A. Singh, L. Harnagea, A. K. Sood, and A. Rao, Ultrafast melting and

- recovery of collective order in the excitonic insulator Ta_2NiSe_5 , *Nature Communications* **12**, 1699 (2021).
- [60] Y.-S. Zhang, J. A. N. Bruin, Y. Matsumoto, M. Isobe, and H. Takagi, Thermal transport signatures of the excitonic transition and associated phonon softening in the layered chalcogenide Ta_2NiSe_5 (2021), [arXiv:2103.13782](https://arxiv.org/abs/2103.13782) [[cond-mat.str-el](#)].
- [61] H. Arima, Y. Naito, K. Kudo, N. Katayama, H. Sawa, M. Nohara, Y. F. Lu, K. Kitagawa, H. Takagi, Y. Uwatoko, and K. Matsubayashi, Resistive anisotropy of candidate excitonic insulator Ta_2NiSe_5 under pressure, *J. Phys.: Conf. Ser.* **1609**, 012001 (2020).
- [62] K. Sun, M. A. Stroscio, and M. Dutta, Graphite c-axis thermal conductivity, *Superlattices and Microstructures* **45**, 60 (2009).